

RESEARCH ARTICLE

10.1002/2017JA024607

Key Points:

- Magnetic pumping of the electron radiation belt is driven by compressions of the dayside magnetosphere combined with pitch angle scattering
- Computer simulations are performed of whistler-chorus-catalyzed and EMIC-catalyzed magnetic pumping in the dayside magnetosphere
- Compressional magnetic pumping contributes to the energization of the electron radiation belt in storms but is not the dominant mechanism

Correspondence to:

J. E. Borovsky,
jborovsky@space.science.org

Citation:

Borovsky, J. E., Horne, R. B., & Meredith, N. P. (2017). The contribution of compressional magnetic pumping to the energization of the Earth's outer electron radiation belt during high-speed stream-driven storms. *Journal of Geophysical Research: Space Physics*, 122, 12,072–12,089. <https://doi.org/10.1002/2017JA024607>




Received 20 JUL 2017

Accepted 7 NOV 2017

Accepted article online 13 NOV 2017

Published online 11 DEC 2017

The Contribution of Compressional Magnetic Pumping to the Energization of the Earth's Outer Electron Radiation Belt During High-Speed Stream-Driven Storms

Joseph E. Borovsky^{1,2} , Richard B. Horne³ , and Nigel P. Meredith³ 

¹CLASP, University of Michigan, Ann Arbor, MI, USA, ²Space Science Institute, Boulder, CO, USA, ³British Antarctic Survey, Cambridge, England

Abstract Compressional magnetic pumping is an interaction between cyclic magnetic compressions and pitch angle scattering with the scattering acting as a catalyst to allow the cyclic compressions to energize particles. Compressional magnetic pumping of the outer electron radiation belt at geosynchronous orbit in the dayside magnetosphere is analyzed by means of computer simulations, wherein solar wind compressions of the dayside magnetosphere energize electrons with electron pitch angle scattering by chorus waves and by electromagnetic ion cyclotron (EMIC) waves. The magnetic pumping is found to produce a weak bulk heating of the electron radiation belt, and it also produces an energetic tail on the electron energy distribution. The amount of energization depends on the robustness of the solar wind compressions and on the amplitude of the chorus and/or EMIC waves. Chorus-catalyzed pumping is better at energizing medium-energy (50–200 keV) electrons than it is at energizing higher-energy electrons; at high energies (500 keV–2 MeV) EMIC-catalyzed pumping is a stronger energizer. The magnetic pumping simulation results are compared with energy diffusion calculations for chorus waves in the dayside magnetosphere; in general, compressional magnetic pumping is found to be weaker at accelerating electrons than is chorus-driven energy diffusion. In circumstances when solar wind compressions are robust and when EMIC waves are present in the dayside magnetosphere without the presence of chorus, EMIC-catalyzed magnetic pumping could be the dominant energization mechanism in the dayside magnetosphere, but at such times loss cone losses will be strong.

1. Introduction

Electrons in the Earth's outer radiation belt are energized during high-speed stream-driven geomagnetic storms to relativistic energies (Borovsky & Denton, 2006; Paulikas & Blake, 1976). Several mechanisms are thought to play a role in this heating, including (a) cyclotron resonance with whistler-mode chorus waves (Horne et al., 2006; Horne, Thorne, Glauert, et al., 2005; Summers et al., 1998), (b) ULF-induced radial diffusion (Mathie & Mann, 2001; Tu et al., 2012), (c) drift resonance with ULF waves (Elkington et al., 1999, 2003; Sauvaud et al., 2013), and (d) substorm field collapse (Dai et al., 2014; Fok et al., 2001; Kim et al., 2000).

The occurrence rate of substorms is high during high-speed stream-driven storms (Borovsky & Yakymenko, 2017). This leads to repeated injections of electrons with energies up to a few hundred keV into the inner magnetosphere (e.g., Borovsky and Denton, 2011; Denton and Borovsky, 2012; Meredith et al., 2011) resulting in whistler-mode chorus wave activity (Meredith et al., 2001, 2002, 2012; Min et al., 2010). Chorus waves accelerate seed electrons, with initial energies of a few hundred keV, up to MeV energies (Horne, Thorne, Glauert, et al., 2005; Horne, Thorne, Shprits, et al., 2005; Thorne et al., 2013), while at the same time leading to loss of lower energy electrons (Artemyev et al., 2015; Horne, Thorne, Glauert, et al., 2005).

Intense levels of radiation belt electrons have been statistically linked to the amplitudes of low-frequency magnetic field fluctuations in the magnetosphere (Kozyreva et al., 2007; Mathie & Mann, 2000; Romanova & Pilipenko, 2009; Rostoker et al., 1998) (although radiation belt correlations with other parameters such as geomagnetic activity, solar wind speed, and solar wind number density are higher (Balikhin et al., 2011; Borovsky & Denton, 2010a; Borovsky, 2017; Borovsky & Denton, 2014; Boynton et al., 2013)). Magnetic field fluctuations in the magnetosphere are found to persist throughout the long durations of high-speed stream-driven

storms (Borovsky & Denton, 2010b), including compressive fluctuations (Borovsky & Denton, 2013; Denton & Borovsky, 2017). ULF waves in the magnetosphere are known to be produced by the buffeting of the magnetosphere by variations in the solar wind dynamic pressure (Borovsky & Denton, 2016; Mathie & Mann, 2001). Radial diffusion (Falthammar & Walt, 1969; Ozeke et al., 2012) and drift-resonant acceleration (Elkington et al., 1999, 2003; Degeling et al., 2008) are two well-studied mechanisms by which magnetospheric ULF waves can affect the evolution of the electron radiation belt. It has been argued that the temporal compressions of the dayside magnetosphere by temporal variations of the solar wind dynamic pressure can lead to collisional magnetic pumping of the radiation belt electrons when pitch angle scattering by plasma waves is present (Borovsky & Denton, 2016; Liu et al., 1999).

Magnetic pumping is a consequence of two simultaneous processes: (1) cyclic magnetic compressions and (2) pitch angle scattering. In the Earth's dayside magnetosphere compression occurs because of the temporal variations in the solar wind ram pressure (Borovsky and Denton, 2010b, 2016; Kepko and Spence, 2003; Li et al., 2013; Viall et al., 2009; Wing and Sibeck, 1997). For radiation belt electrons in the dayside magnetosphere, pitch angle scattering is believed to be produced by whistler-mode chorus outside of the plasmasphere (Shprits et al., 2007; Thorne et al., 2005), by electromagnetic ion cyclotron waves inside and outside the plasmaspheric drainage plume (Jordanova et al., 2006; Kovalevskiy, 1980, 1981; Spasojevic and Fuselier, 2009; Thorne et al., 2006), and by whistler-mode hiss (Chan & Holzer, 1976; Summers et al., 2008) inside the plasmaspheric drainage plume and the plasmasphere.

In this study the role of compressions of the dayside magnetosphere on the energization of the electron radiation belt is investigated. Specifically, the role of compressions with timescales slower than ULF periods is examined; these compressions are owed to temporal changes in the ram pressure of the solar wind caused by structure in the solar wind plasma advecting past the Earth (Borovsky & Denton, 2016). (Dayside compressions might also be caused by foreshock transients upstream of the Earth; e.g., Hartinger et al., 2013; Safrankova et al., 2012). These compressions are not periodic in time but are irregular. In the magnetic pumping process the energy for the energization of radiation belt electrons comes from the solar wind compressions.

In this report computer simulations of the magnetic pumping process will be driven by spacecraft measurements of magnetic field compressions in the dayside magnetosphere during high-speed stream-driven storms. The time-dependent magnetic field strength $B(t)$ that a particle experiences in the nightside magnetosphere is too difficult to estimate (cf. section 6 of Borovsky and Denton, 2016); measured values of the changes in the magnetic field strength ΔB are very large at geosynchronous orbit in the nightside (Borovsky & Denton, 2010b), and some of the time variation of the field strength is owed to the movement of gradients in the magnetic field morphology at the dipole-tail transition. Hence, in this report the focus will be on the compressional magnetic pumping of radiation belt electrons in the dayside magnetosphere.

The objective of this simulation study is to assess the contribution of magnetic pumping to the energization of the outer electron radiation belt, especially in comparison with chorus energy diffusion. To accomplish this the simulations will be kept simple and focused on magnetic pumping and on energy diffusion. Among the processes that will not be included in the simulations are (1) radial diffusion by ULF waves, (2) radial diffusion by the combined action of shell splitting and pitch angle scattering, (3) time dependence in the amplitudes of whistler-mode chorus waves and electromagnetic ion cyclotron (EMIC) waves, (4) the time dependence of the substorm-injected electron population at tens to hundreds of keV, and (5) strongly increased electron loss due to combined effects of EMIC and chorus waves, even if these waves occur at different magnetic local times (e.g., Mourenas et al., 2016).

This study is organized as follows. In section 2 the magnetic pumping process is explained. In section 3 the computational methods that are used to simulate magnetic pumping are discussed along with the magnetic field compressions used as input to the simulations (section 3.1) and the values taken for pitch angle diffusion coefficients (section 3.2) for whistler-mode chorus waves and for EMIC waves. In section 4 the simulation results are discussed for initial-value-problem simulations (no fixed seed population) in section 4.1 and for boundary value problem simulations (with a constant seed population) in section 4.2. In section 5 the simulation results for magnetic pumping are compared with energy diffusion for whistler-mode chorus. Section 6 contains discussions about the efficiency of magnetic pumping for energizing the outer electron radiation belt, about the action of magnetic pumping during coronal mass ejection (CME) sheath-driven storms, and about the magnetic pumping of the outer proton radiation belt. The findings of this study are summarized in section 7.

2. Compressional Magnetic Pumping

Magnetic pumping (Alfvén, 1950; Schluter, 1957; Spitzer & Witten, 1953) is an interplay between cyclic magnetic compressions and pitch angle scattering. In the absence of scattering, charged particles behave adiabatically in the cyclic compressions and no net particle energization occurs. Pitch angle scattering breaks the adiabaticity of the particles and allows the cyclic compressions to systematically heat the particles. If the two processes occur simultaneously, then some degree of heating is unavoidable. Basic explanations of the magnetic pumping process can be found in Alfvén and Fälthammar (1963) and Borovsky (1986). Magnetic pumping has been invoked to explain the heating of ions and electrons in the rapidly rotating magnetosphere of Jupiter (Borovsky et al., 1981; Goertz, 1978; Mu, 1993) and to contribute to the energization of particles in the Earth's magnetosphere (Alfvén, 1959; Dmitriev et al., 2001; Liu & Rostoker, 1995; Liu et al., 1999).

Note that the term “magnetic pumping” is also used in plasma physics to denote transit-time processes (e.g., Canobbio, 1972; Koechlin and Samain, 1971; Kuijpers et al., 1997; Tataronis and Grossmann, 1976): to avoid confusion in this report the term “compressional magnetic pumping” will be used. Compressional magnetic pumping has also been denoted as “collisional magnetic pumping” and as the “gyrorelaxation effect.”

The energization timescale for compressional magnetic pumping depends on three parameters: (1) $\Delta B/B$ the fractional strength of the magnetic compression, (2) τ_{cycle} the cycle time of the compression, and (3) τ_{scat} the pitch angle scattering timescale. Applying magnetic pumping to electrons in the dayside magnetosphere will involve compression cycle times τ_{cycle} in the range of 5–20 min, pitch angle scattering times τ_{scat} in the range of 10–1,000 min, and compression amplitudes $\Delta B/B$ in the range of 0.05–0.2.

Analysis in the literature demonstrates that magnetic pumping will heat (i.e., increase the average kinetic energy of) a population of particles (e.g., Alfvén, 1954; Murty and Varma, 1958). Through the randomness of the pitch angle scattering process, magnetic pumping also results in a momentum diffusion (energy diffusion) of the particle population (cf. Borovsky et al., 1981; Borovsky, 1986, 1988; Liu et al., 1999; Melrose, 1969), which results in the rapid production of a high-energy tail on the distribution of particles.

3. Simulation Methods

The magnetic pumping simulations follow the evolution in momentum p versus equatorial pitch angle α space of all of the electrons in a magnetic flux tube in the dayside magnetosphere. Electrons of different kinetic energies cross the dayside magnetosphere at different azimuthal speeds, and a given set of electrons with diverse kinetic energies will not stay in the same flux tube. However, as electrons of a given kinetic energy exit the flux tube, other electrons of the same kinetic energy will enter the flux tube maintaining a distribution function within that flux tube. Rather than considering the electron content of a dayside magnetic flux tube, one could think of the simulations as following the evolution of the electron content of an entire dayside flux surface.

Simulations are run, typically, for a 24 h long interval driven by a time series of spacecraft measurements of the magnetic field strength in the dayside magnetosphere at geosynchronous orbit (Figure 1, which is described in section 3.2). Electrons of different kinetic energies orbit the Earth at different speeds, but each energetic electron spends approximately the same fraction of a day in the dayside magnetosphere. Since azimuthal angular drift speeds tend to be higher on the nightside than on the dayside (cf. sections 1.6 and 3.3 of Roederer and Zhang, 2014), electrons spend more than half a day in the dayside magnetosphere during 1 day of elapsed time.

The global magnetic field strength changes in the dayside magnetosphere are associated with changes in the intensity and the radial location of the Chapman-Ferraro current on the dayside magnetopause. Electron guiding centers move with magnetic flux surfaces in the induction electric fields associated with temporal changes in the magnetic field strength $\partial \vec{B} / \partial t$ so that (1) the electron experiences a change in the field strength $\Delta B = \int (dB/dt) dt$ and (2) μ is conserved for the electron, as long as the timescale of the field change is longer than the electron gyroperiod (Borovsky and Hansen, 1990, 1991). These two things are true regardless of the electron's kinetic energy. Electrons with kinetic energies of 1 MeV or more cross the dayside magnetosphere in about 2–5 min or less. For dayside field compressions that are slower than these crossing times, the relativistic electrons make one or more passes across the dayside magnetosphere during a single slow compression and make one or more passes across the dayside magnetosphere during a single slow decompression. Each time the electron passes through the dayside, it experiences a change in the field strength that is roughly

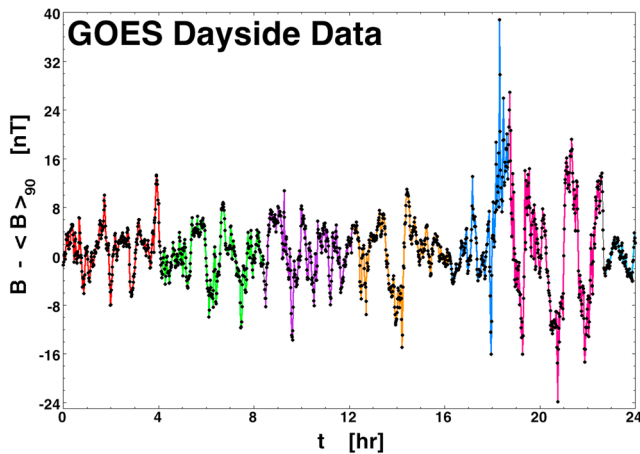


Figure 1. The time series of spacecraft-measured magnetic compressions in the dayside magnetosphere used to drive the magnetic pumping computer simulations. Each color is data from one pass of a GOES spacecraft between 10 and 14 h local time.

$\tau_{\text{cross}} dB/dt$ where τ_{cross} is the dayside crossing time and dB/dt is the rate of field change on the electron's flux surface. While the electron is crossing the nightside magnetosphere, it may not be experiencing a change in the magnetic field strength, depending on what the inductive electric field in the nightside is. Ignoring the complexity of what may be happening in the nightside magnetosphere, for slow compressions the compression efficiency may be reduced by a factor of 2 for very energetic electrons since the electron is only in the dayside about half of the time and only experiences half of time-integrated ΔB . Hence, the magnetic pumping efficiencies may be reduced for high-energy electrons in slow compression: this is not accounted for in the simulations. Fortunately, the magnetic field time series of Figure 1 is dominated by faster compressions, wherein the magnetic pumping efficiency of very energetic electrons is less reduced. (Note that fast compressions are still slow compared with electron gyroperiods and electron bounce periods.)

A further approximation made in this very basic assessment of magnetic pumping is that radial diffusion associated with the combined action of pitch angle scattering and shell splitting (e.g., Borovsky et al., 2014; Falthammar and Walt, 1969; Roederer and Schulz, 1969) is ignored: pitch angle scattering is accounted for but shell splitting is ignored.

3.1. The Magnetic Pumping Simulation Code

To examine the contribution of compressional magnetic pumping to the evolution of the outer electron radiation belt during high-speed stream-driven storms, numerical simulations of the magnetic pumping of the electron radiation belt population are performed using the magnetic pumping simulation code described in the Appendix of Borovsky et al. (1981). The evolution of electron distribution functions under the action of the compressional magnetic pumping process is simulated by advecting and diffusing elements of the distribution function on a two-dimensional grid in momentum versus pitch angle space (cf. Borovsky, 1986; Borovsky et al., 1981). The simulation grid is shown in Figure 2, with coordinates $p = \gamma m_e v$ (horizontal) and equatorial pitch angle α (vertical). The simulations operate on the quantity

$$n(p, \alpha) = 2 v \tau_b \sin \alpha \cos \alpha f(p, \alpha) , \quad (1)$$

where $n(p, \alpha) dp d\alpha$ is the number of electrons in a flux tube with momentum p and equatorial pitch angle α , where $f(p, \alpha)$ is the phase-space distribution of the electrons (assumed to be gyrotropic), where v is the velocity of an electron with momentum p , and where $\tau_b(\alpha)$ is the pitch angle-dependent portion of the electron bounce time in a dipole magnetic field, approximated as $\tau_b(\alpha) \approx 1.30 - 0.56 \sin \alpha$ in units of seconds (Hamlin et al., 1961; Lyons et al., 1972). In the sketch of Figure 2 the coordinates of a typical simulation are shown with α going from 0° to 90° and with momentum p going from 0 to $21 m_e c$. The kinetic energies of electrons

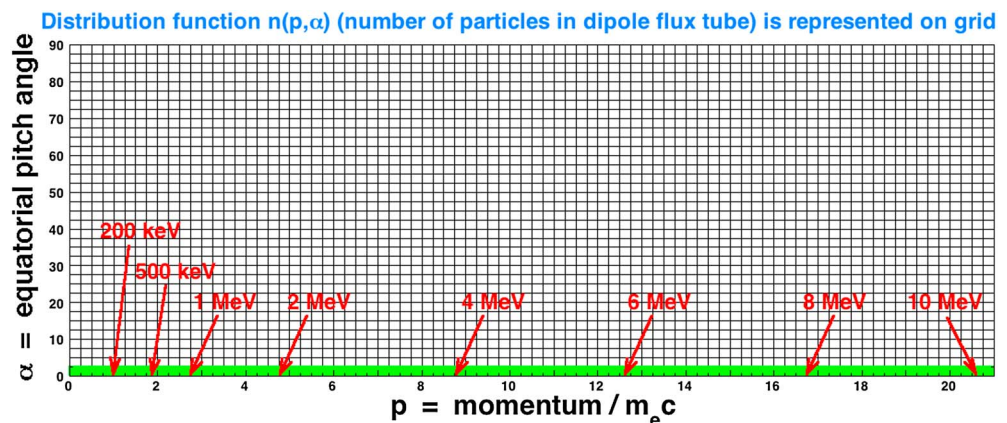


Figure 2. A sketch of the two-dimensional p - α grid used for the simulations of compressional magnetic pumping. A typical grid used for the simulations is $2,401 \times 91$ grid points in p and α .

$E = (\gamma - 1)m_e c^2$ are denoted with the red arrows in Figure 2. The green shading on the grid denotes the extent of the atmospheric loss cone. (Note that the deviation of the loss cone away from the equatorial pitch angle $\alpha = 0^\circ$ (cf. Porazik et al., 2014), which becomes important at geosynchronous orbit for electrons with energy of about 10 MeV and higher, is not accounted for in the simulations.) A typical simulation uses a grid that is 2,401 grid spaces in p and 91 grid spaces in α .

To account for the evolution of the electron distribution function under the action of compression and decompression, the elements of the distribution $n(p, \alpha)$ are advected in p - α space conserving the first and second adiabatic invariants μ and J for motion in a dipolar magnetic field as the magnetic field strength changes (Borovsky et al., 1981; Goertz, 1978). When the magnetic field strength B increases, conservation of $\mu = p_\perp^2/B$ causes the elements of $n(p, \alpha)$ to advect to higher values of p and to larger values of α ; a decrease of the magnetic field strength leads to advection to lower values of p and smaller values of α . A conservative advection scheme is used that moves the values of the distribution $n(p, \alpha)$ on the grid points forward in time and then linearly interpolates those values onto an updated p - α grid. As will be quantified in section 4.1, this advection scheme introduces a numerical diffusion into the simulations.

Pitch angle scattering is implemented by numerically solving the bounce-averaged pitch angle diffusion equation (cf. equation (10) of Lyons et al., 1972)

$$\frac{\partial f}{\partial t} = \frac{1}{\tau_b(\alpha) \sin \alpha \cos \alpha} \frac{\partial}{\partial \alpha} \left[\tau_b(\alpha) \sin \alpha \cos \alpha D_{\alpha\alpha} \frac{\partial f}{\partial \alpha} \right] \quad (2)$$

with energy-dependent pitch angle diffusion coefficients $D_{\alpha\alpha}(p, \alpha)$ calculated for the observed spectra of chorus waves and EMIC waves near geosynchronous orbit (cf. section 3.3). Using expression (1) and defining

$$H(p, \alpha) = -D_{\alpha\alpha}(p, \alpha) \frac{\partial}{\partial \alpha} [\log(\tau_b \sin \alpha \cos \alpha)] \quad , \quad (3)$$

(where $\tau_b = 1.30 - 0.56 \sin \alpha$ is a function of α), expression (2) becomes

$$\frac{\partial n}{\partial t} = \frac{\partial}{\partial \alpha} \left[D_{\alpha\alpha} \frac{\partial n}{\partial \alpha} \right] + \frac{\partial}{\partial \alpha} [Hn] \quad , \quad (4)$$

where n , H , and $D_{\alpha\alpha}$ are all functions of p and α . In the simulations expression (4) is implicitly solved with an iterative tridiagonal algorithm as outlined in Appendix 1 of Borovsky et al. (1981).

In the computer simulations the two processes (magnetic compression and pitch angle scattering) are temporally interleaved with a small change in the field strength B implemented, then the pitch angle scattering for the small time increment is implemented, and the compression-scattering cycle is repeated. A time step of 1 min is used for the change in the magnetic field strength, followed by 1 min of pitch angle scattering. This 1 min time step is shorter than the timescale for strong diffusion.

3.2. Magnetic Field Compressions $\Delta B/B$ of the Dayside Magnetosphere

Temporal compression of the dayside magnetic field of the Earth was analyzed by Borovsky and Denton (2016). Measurements of the magnetic field strength $B(t)$ at geosynchronous orbit in the dayside magnetosphere were examined and compared with a mathematical model of the compression of the dayside magnetic field by temporal variations in the solar wind. The radial motions of flux surfaces in the dayside magnetosphere were followed in the compression model. Because electrons move radially with flux surfaces, it was concluded in Borovsky and Denton (2016) that the particles in the dayside magnetosphere experience a magnetic field temporal compression that is about twice as large as the magnetic field strength change measured by a spacecraft.

The quantity $\Delta B/B$ (where B is the magnetic field strength $|\vec{B}|$) is the quantity that is relevant for the description of plasma compressions and decompressions. For the simulations, measurements of the magnetic field strength $B(t)$ in the dayside magnetosphere from the GOES spacecraft are used. For the GOES spacecraft in geosynchronous orbit, long continuous data intervals from the dayside magnetosphere are not obtained, so multiple intervals from multiple dayside passes are strung together in time to produce a longer continuous interval of $B(t)$. In Figure 1 one such long interval is plotted. To determine the time variation of B and to remove the systematic local time variation in the baseline of the magnetic field strength, the quantity $\Delta B = B(t) - \langle B(t) \rangle_{90}$ is determined from the GOES measurements where $\langle B(t) \rangle_{90}$ is the 90 min running average of $B(t)$. In Figure 1 $\Delta B = B(t) - \langle B(t) \rangle_{90}$ is plotted with 1-min time resolution for 1 day of time,

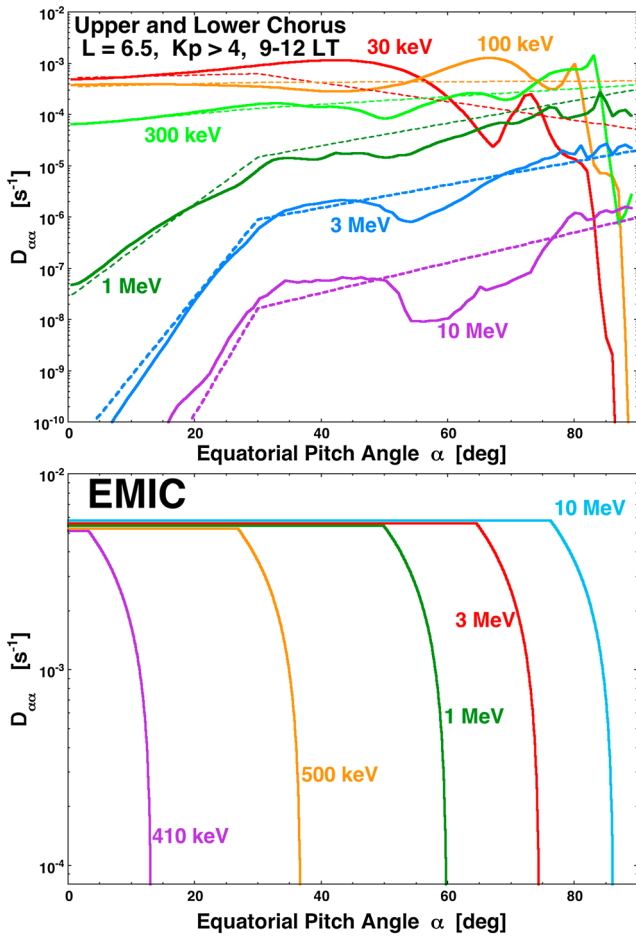


Figure 3. Bounce-averaged pitch angle diffusion coefficients $D_{\alpha\alpha}$ for electrons (in units of $\text{radians}^2 \text{ s}^{-1}$) in the dayside magnetosphere are plotted as functions of the equatorial pitch angle. (top) The solid curves are calculated $D_{\alpha\alpha}$ values for whistler-mode chorus waves from Horne et al. (2013), and the dashed curves are algebraic parameterizations of the calculated values. (bottom) The solid curves are parameterizations of the $D_{\alpha\alpha}$ values for EMIC waves from Figure 3c of Ukhorskiy et al. (2010).

constructed from seven passes of GOES 10 and GOES 12 across the dayside magnetosphere (from 10 to 14 local time) during the first day of several high-speed stream-driven storms in the year 2003. Each separate spacecraft pass is plotted in a different color, and the data from one pass to the next are connected via a linear interpolation over a 5 min period. To get $\Delta B/B$ for the magnetic pumping simulations, the measured quantity $\Delta B = B(t) - \langle B(t) \rangle_{90}$ is multiplied by 2 to account for the fact that particles in the dayside magnetosphere experience approximately twice the magnetic compression as measured by a stationary spacecraft (Borovsky & Denton, 2016). This $2\Delta B$ is then divided by $B_0 = 110 \text{ nT}$, a typical magnetic field strength in the dayside magnetosphere at geosynchronous orbit.

3.3. Pitch Angle Diffusion Coefficients $D_{\alpha\alpha}$

To simulate the pitch angle scattering of electrons by whistler-mode chorus waves, the bounce-averaged pitch angle diffusion coefficients $D_{\alpha\alpha}(p, \alpha)$ calculated for whistler-mode chorus waves by Horne et al. (2013) are algebraically parameterized. Those $D_{\alpha\alpha}$ coefficients are plotted as the solid curves in Figure 3 (top), and the algebraic $D_{\alpha\alpha}$ parameterizations are plotted as the dashed curves in Figure 3 (top). The $D_{\alpha\alpha}(p, \alpha)$ coefficients are for a combination of upper band and lower band chorus emission in the 9–12 LT sector at $L^* = 6.5$ and $Kp > 4$. The algebraic parameterization of the pitch angle diffusion coefficients $D_{\alpha\alpha}(p, \alpha)$ is given by

$$D_{\alpha\alpha} = 10^{-Q} \quad (5a)$$

$$Q = C_0 + \frac{\alpha}{30^\circ} (C_{30} - C_0) \quad \text{for } \alpha \leq 30^\circ \quad (5b)$$

$$Q = C_{30} + \frac{\alpha - 30^\circ}{60^\circ} (C_{90} - C_{30}) \quad \text{for } \alpha \geq 30^\circ \quad (5c)$$

$$C_0 = 2.787 + 0.333 \log_{10}(E) \quad \text{for } E \leq 251 \text{ keV} \quad (5d)$$

$$C_0 = -11.7 + 6.42 \log_{10}(E) \quad \text{for } E \geq 251 \text{ keV} \quad (5e)$$

$$C_{30} = 3.196 + 0.746 (\log_{10}(E) - 1.524)^2 \quad (5f)$$

$$C_{90} = 10.07 - 3.897 \log_{10}(E) \quad \text{for } E \leq 56 \text{ keV} \quad (5g)$$

$$C_{90} = 3.02 + 0.16 \log_{10}(E) \quad \text{for } 56 \text{ keV} \leq E \leq 1 \text{ MeV} \quad (5h)$$

$$C_{90} = -4.0 + 2.5 \log_{10}(E) \quad \text{for } E \geq 1 \text{ MeV}, \quad (5i)$$

where $D_{\alpha\alpha}(p, \alpha)$ is in units of radian^2/s , where E is the electron energy in units of keV, and where α is the equatorial pitch angle of the electron in degrees.

To simulate the pitch angle scattering of electrons by electromagnetic ion cyclotron (EMIC) waves in the plasmaspheric drainage plume of the dayside magnetosphere (cf. Borovsky et al., 2014) (or in the dayside magnetosphere in general), the bounce-averaged pitch angle diffusion coefficients $D_{\alpha\alpha}(p, \alpha)$ calculated for EMIC waves by Ukhorskiy et al., 2010 are algebraically parameterized for use in the magnetic pumping code. Using Figure 3c of Ukhorskiy et al. (2010), the following parameterization is used:

$$D_{\alpha\alpha} = D_0 \quad \text{for } \alpha \leq \alpha_1 \quad (6a)$$

$$D_{\alpha\alpha} = D_0 \frac{(\alpha_2 - \alpha)}{10^\circ} \quad \text{for } \alpha_1 \leq \alpha \leq \alpha_2 \quad (6b)$$

$$D_{\alpha\alpha} = 0 \quad \text{for } \alpha \geq \alpha_2 \quad (6c)$$

$$\alpha_2 = 85^\circ \frac{E^*}{E^* + 23.4} + \frac{E}{1,360} \quad \text{for } E \geq 400 \text{ keV} \quad (6d)$$

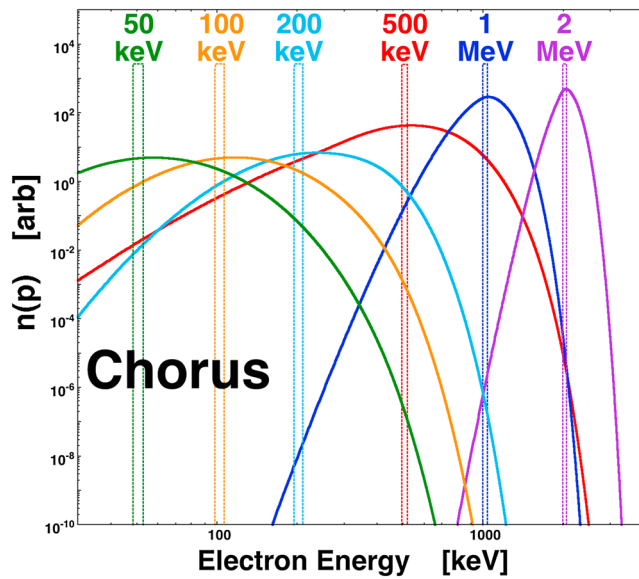


Figure 4. Six initial value simulations of compressional magnetic pumping of electrons catalyzed by whistler-chorus pitch angle scattering. The six dashed curves are the initial energy distributions (isotropic in pitch angle) of electrons in the six simulations, and the six solid curves are the electron energy distributions after 1 day of compressional magnetic pumping. The simulation grids were $2,401 \times 91$ grid points in p and α . The atmospheric loss cone was operating in all of the simulations, and the plotted curves are integrated over all pitch angles.

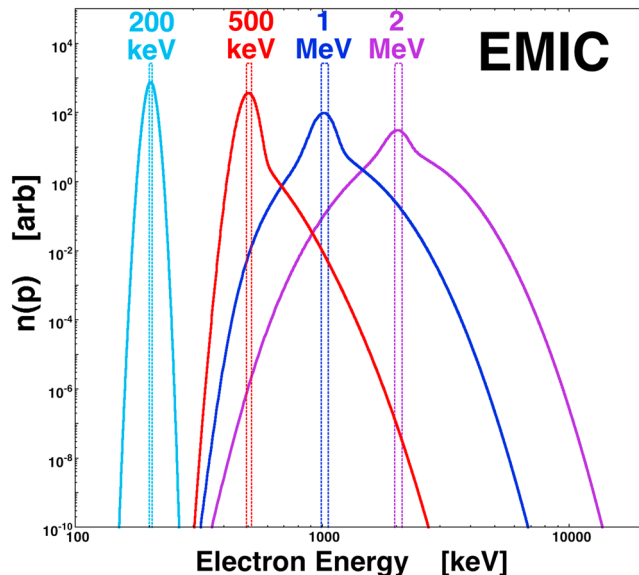


Figure 5. Four initial value simulations of compressional magnetic pumping of electrons catalyzed by EMIC pitch angle scattering. The four dashed curves are the initial energy distributions (isotropic in pitch angle) of electrons in the four simulations, and the four solid curves are the electron energy distributions after 1 day of compressional magnetic pumping. The simulation grids were $3,601 \times 91$ grid points in p and α . The atmospheric loss cone was operating in all of the simulations, and the plotted curves are integrated over all pitch angles.

$$\alpha_2 = 0^\circ \quad \text{for } E < 400 \text{ keV} \quad (6e)$$

$$\alpha_1 = \alpha_2 - 10^\circ \quad (6f)$$

$$E^* = (E - 400)^{0.622}, \quad (6g)$$

where $D_{\alpha\alpha}(p, \alpha)$ is in units of radian^2/s , where E is the electron energy in units of keV, and where α is the equatorial pitch angle of the electron in degrees. The parameterized values of $D_{\alpha\alpha}(p, \alpha)$ are plotted as the solid curves in Figure 3 (bottom) for the value $D_0 = 5.8 \times 10^{-3} \text{ radians}^2 \text{ s}^{-1}$. For most simulations the value $D_0 = 500 \text{ radians}^2 \text{ d}^{-1} = 5.8 \times 10^{-3} \text{ radians}^2 \text{ s}^{-1}$ (cf. Albert, 2008, 2010) is used.

4. Simulation Results

To study the energization of the outer electron radiation belt by compressional magnetic pumping, simulations are run in two manners: as initial value problems and as boundary value problems. Initial-value-problem simulations (section 4.1) start out with an initial energy distribution of electrons and evolve that distribution in time without the presence of a continuously maintained population of seed electrons. Boundary-value-problem simulations (section 4.2) specifically maintain a population of low-energy electrons (maintaining a boundary condition on the low-energy portion of the distribution function) and track in time the evolution of higher-energy electrons from this seed population.

For all cases, the magnetic field strength temporal profile used in the simulations is the composite created from measurements by GOES 10 and GOES 12 in the dayside magnetosphere in geosynchronous orbit (Figure 1), as described in section 3.2. The magnetic field strength changes once per minute for 1 day (1,440 min). The pitch angle scattering in the simulations is implemented from either the upper and lower band chorus wave diffusion coefficients or from the dayside EMIC wave pitch angle diffusion coefficients, as described in section 3.3. In all cases the atmospheric loss cone is active in the simulations.

4.1. Initial-Value-Problem Simulations

In the initial-value-problem simulations, the evolution of an initial energy distribution of electrons is followed in time. The initial distributions are isotropic in pitch angle. A narrow energy slice is used in each simulation in order to determine the action of magnetic pumping on the various energy ranges in the outer electron radiation belt and in the population of lower energy seed electrons.

In Figure 4 the evolution of six narrow energy slices is shown after 24 h of chorus-catalyzed compressional magnetic pumping from six separate simulations. In Figure 4 the pitch angle scattering of the electrons is by whistler-mode chorus waves. These six simulations are plotted in six different colors. For the six simulations the initial ($t = 0$) energy distributions are plotted as the dashed curves, and the final ($t = 1$ day) distributions are plotted as the solid curves. The plotted distributions are integrated over all pitch angles. Note in Figure 4 that all six cases show a significant spread in energies after 1 day of magnetic pumping with production of electron energies that are much higher than the initial energies. Note that there is also spreading of the electron distributions to lower energies. Because the chorus wave pitch angle scattering is faster at lower energies (i.e., $D_{\alpha\alpha}$ is larger at lower energies as shown in Figure 3), the magnetic pumping

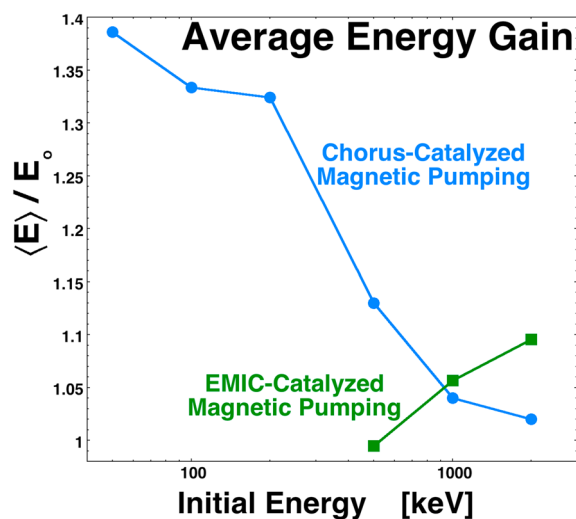


Figure 6. For the initial-value-problem simulations of Figures 5 and 6, the fractional energy gain of the electron distributions after 1 day of compressional magnetic pumping is plotted as a function of the initial energy of the electrons. The blue curve is for whistler-chorus catalyzed magnetic pumping, and the green curve is for EMIC-catalyzed magnetic pumping.

grid points. What was a delta function in density is spread in the p direction and in the α direction. In the p direction the average distance of spreading is $0.5 \delta p$ each time the distribution is advected, where δp is the numerical grid spacing in the p direction. Repeated advectations result in repeated spreading. A numerical diffusion coefficient in the p direction can be constructed: $D_{\text{numerical}} = (0.5 \delta p)^2 / \delta t$, where δt is the advection time step. Using $\partial f / \partial t = D_{\text{numerical}} \partial^2 f / \partial p^2$, the spread Δp in the momentum direction in a time $t = 1$ day = 1,440 δt advection steps can be approximated by $\Delta p = (D_{\text{numerical}} t)^{1/2} = [(0.5 \delta p)^2 1,440] = 19 \delta p$. Hence, in a 24 h simulation numerical diffusion will spread an initial shape by about 19 grid spaces in each direction, increasing a narrow slice to about 38 grid spaces. That is the amount of momentum spreading seen in the blue curve of Figure 5. In the magnetic pumping simulations, numerical diffusion is controlled by using a grid with small grid spaces δp in the momentum p direction; this requires a lot of grid points in the p direction on the numerical mesh. (Typically, 2,401 grid spaces in p are used, and on occasion 3,601 grid spaces.)

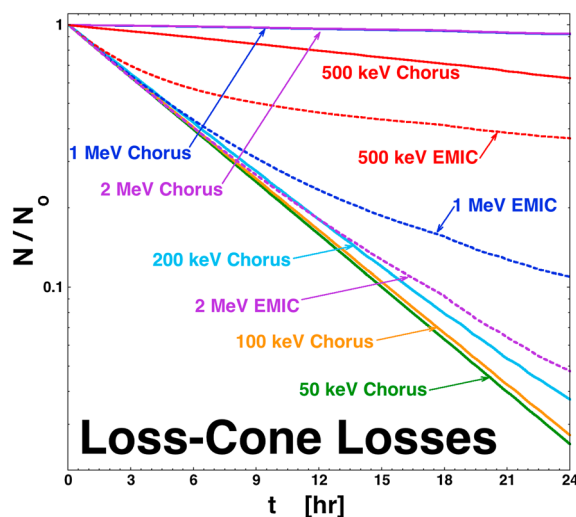


Figure 7. For the initial-value-problem simulations of Figures 5 and 6, the loss rate of electrons into the atmospheric loss cone is plotted as a function of time for 1 day of compressional magnetic pumping. The solid curves are for whistler-chorus waves producing the pitch angle scattering in the simulations, and the dashed curves are for EMIC waves producing the pitch angle scattering in the simulations.

process is more efficient at lower energies. This results in a larger spread in energies for electrons starting out at lower energies: for example, the 50 keV initial distribution (green) in Figure 4 evolves to energies of several times 50 keV whereas the 2 MeV initial energy distribution (purple) evolves to only about twice 2 MeV.

In Figure 5 the evolution of four electron energy slices are plotted after 1 day of EMIC-catalyzed compressional magnetic pumping with EMIC waves producing the pitch angle scattering. The four simulations are plotted in four different colors; all plotted curves are integrals of all pitch angles. Again, the dashed curves are the initial ($t = 0$) energy distributions, and the solid curves are the final ($t = 1$ day) energy distributions. At energies below 400 keV the EMIC pitch angle diffusion coefficients $D_{\alpha\alpha}$ are zero, so magnetic pumping should not act on electrons with energies below 400 keV when EMIC provides the scattering. The spread in the 200 keV distribution (light blue curve in Figure 5) at $t = 1$ day is produced by numerical diffusion in the advection scheme of the magnetic pumping simulation code. The numerical diffusion in momentum (energy) works as follows. When the magnetic field strength changes, each element of the electron distribution function that is exactly on each p - α grid point is advected to a new location in p and α (conserving two adiabatic invariants). That new location is not exactly on a grid point, so the electron distribution advected to the new location is linearly interpolated onto the four nearest

grid points. What was a delta function in density is spread in the p direction and in the α direction. In the p direction the average distance of spreading is $0.5 \delta p$ each time the distribution is advected, where δp is the numerical grid spacing in the p direction. Repeated advectations result in repeated spreading. A numerical diffusion coefficient in the p direction can be constructed: $D_{\text{numerical}} = (0.5 \delta p)^2 / \delta t$, where δt is the advection time step. Using $\partial f / \partial t = D_{\text{numerical}} \partial^2 f / \partial p^2$, the spread Δp in the momentum direction in a time $t = 1$ day = 1,440 δt advection steps can be approximated by $\Delta p = (D_{\text{numerical}} t)^{1/2} = [(0.5 \delta p)^2 1,440] = 19 \delta p$. Hence, in a 24 h simulation numerical diffusion will spread an initial shape by about 19 grid spaces in each direction, increasing a narrow slice to about 38 grid spaces. That is the amount of momentum spreading seen in the blue curve of Figure 5. In the magnetic pumping simulations, numerical diffusion is controlled by using a grid with small grid spaces δp in the momentum p direction; this requires a lot of grid points in the p direction on the numerical mesh. (Typically, 2,401 grid spaces in p are used, and on occasion 3,601 grid spaces.) The other 1 day curves in Figure 5 have unusual shapes, with two components, which are explained as follows. In the simulations the initial energy slices are taken to be isotropic in equatorial pitch angle; hence, there are initial electrons with all pitch angles from $\alpha = 0^\circ$ to $\alpha = 90^\circ$. For EMIC waves, the pitch angle diffusion coefficients $D_{\alpha\alpha}(\alpha)$ are zero near $\alpha = 90^\circ$ (cf. Figure 3, bottom). This is particularly true for $E = 500$ keV electrons where (cf. expressions (6c) and (6d)) $D_{\alpha\alpha}(\alpha) = 0$ for $36.8^\circ \leq \alpha \leq 90^\circ$. The initial electrons in the $36.8^\circ \leq \alpha \leq 90^\circ$ range will not take part in the magnetic pumping process, but they will numerically diffuse as they are advected on the p - α grid as the magnetic field changes with time. For the two-component distributions of Figure 5, the narrow component is composed of the initial electrons that are not being pumped. The broad component is composed of the initial electrons that are caught up in the magnetic pumping process.

Examining Figures 4 and 5, two general conclusions about the production of energetic tails on the energy distributions are (1) that chorus-catalyzed magnetic pumping is more efficient at lower energies than it is at high energies and (2) that EMIC-catalyzed magnetic pumping is more effective at higher energies than it is at lower energies. Further (depending of course on the amplitudes of the chorus and the EMIC), EMIC tends to be more

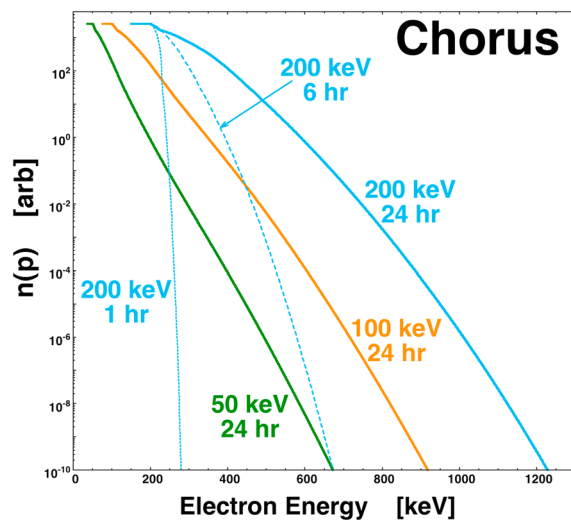


Figure 8. Three boundary value simulations of compressional magnetic pumping of electrons catalyzed by whistler-chorus pitch angle scattering. In the boundary value simulations a constant supply of low-energy electrons is maintained. In the three simulations the maximum energy of the maintained distribution is 50 keV (green curve), 100 keV (orange curve), and 200 keV (light blue curves). The three solid curves are the electron energy distributions after 1 day of compressional magnetic pumping. The simulation grids were 2401×91 grid points in p and α , the atmospheric loss cone was operating in all of the simulations, and the plotted curves are integrated over all pitch angles.

effective than chorus at enabling the magnetic pumping of high-energy radiation belt electrons.

For the initial-value-problem simulations of Figures 4 and 5, the 1 day change in the average energy of the electron distribution is plotted as a function of the initial energy of the electrons in Figure 6. The vertical axis is the mean energy of the electrons $\langle E \rangle$ after 1 day of pumping divided by the initial energy of the electrons E_0 . This is akin to a “heating rate” for the population. In Figure 6 the blue curve is for chorus-catalyzed magnetic pumping, and the green curve is for EMIC-catalyzed magnetic pumping. Note that there are loss cone losses of electrons in the simulations and that these mean energies $\langle E \rangle$ are the mean energies of the electrons that survive. The chorus-catalyzed magnetic pumping (blue) shows a much stronger fractional heating rate for what might be considered the seed population of electrons for the radiation belt, energies of 50–200 keV. According to Figure 6 the mean energy of those electrons increases by 30%–40% after 1 day of magnetic pumping. For example, a 1 day heating rate of 32% for 200 keV electrons in Figure 6 corresponds to an average energy increase of 62 keV per day per electron. Much of this increase of the mean energy is owed to the stronger loss cone losses at lower energies leaving predominantly higher energies. In Figure 6, for higher initial energies the rate of heating is more modest, about 5%–10% after 1 day of chorus-catalyzed magnetic pumping. The heating rates for EMIC-catalyzed magnetic pumping (green curve) are also modest, about 0% to 10% after 1 day. Note that the value of $\langle E \rangle / E_0$ for EMIC is in part dependent on the fraction of the initial electrons that do not take part in the magnetic pumping process because their initial pitch angles are too great, which is significant for $E_0 = 500$ keV.

In Figure 7 the loss of electrons into the loss cone is examined for the initial-value-problem simulations of Figures 4 and 5. Here the ratio of the integral $\int \int n(p, \alpha) d\alpha dp$ of the energy distribution function N at time t to the integral of the initial energy distribution function N_0 at time $t = 0$ is plotted as a function of time in the simulations. For lower energy electrons subject to pitch angle scattering by chorus waves the loss of electrons from the simulation is substantial. At higher energies for scattering by chorus the loss rates into the atmosphere are small. As can be seen in Figure 3 $D_{\alpha\alpha}(\alpha)$ is small near $\alpha = 0^\circ$ at higher energies, so electron pitch angle scattering into the loss cone is slow. For EMIC waves the pitch angle diffusion coefficient $D_{\alpha\alpha}(\alpha)$ is robust near $\alpha = 0^\circ$, so electrons flow strongly into the atmospheric loss cone in the EMIC-catalyzed simulations. Note in Figure 7 that the loss rate of 500 keV electrons under EMIC (red dashed curve) is not as strong as the loss rates of 1 MeV and 2 MeV initial electrons under EMIC (blue dashed and purple dashed curves); this is because a substantial portion of the initial 500 keV electrons are not subject to pitch angle scattering since $D_{\alpha\alpha}(\alpha) = 0$ for EMIC for $\alpha \geq 36.8^\circ$ at 500 keV, and those electrons are not lost (neither are they energized by magnetic pumping: see the narrow distributions in Figure 5).

4.2. Boundary-Value-Problem Simulations

The magnetic pumping simulations are run in a boundary value fashion to examine the production of energetic electrons from a constant (in time) population of lower energy seed electrons. The idea is that the seed electrons (cf. Borovsky, 2017; Friedel et al., 2002; McDiarmid and Burrows, 1965) are constantly injected into the dipolar magnetosphere by substorms that occur throughout the duration of a high-speed stream-driven storm. At geosynchronous orbit, substorm-injected electrons have typical kinetic energies of 50 to 300 keV (Birn et al., 1998, 2000; Cayton et al., 1989; Denton et al., 2010; Lezniak et al., 1968), although under special circumstances electrons with energies of 1 MeV can be injected by substorms (cf. Borovsky et al., 2016; Ingraham et al., 2001).

Figure 8 shows the results of three simulations: (1) when a population of electrons is maintained at $E \leq 50$ keV (green curve), (2) when a population of electrons is maintained at $E \leq 100$ keV (orange curve), and (3) when a population of electrons is maintained at $E \leq 200$ keV (blue curves). The energy distribution functions (integrated over all pitch angles) in the three simulations are shown after 24 h of chorus-catalyzed magnetic

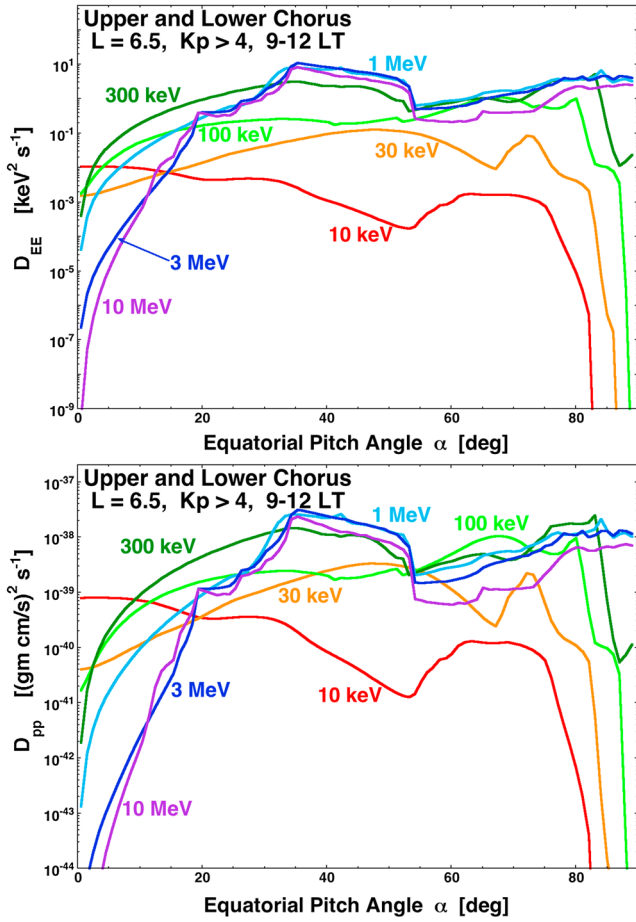


Figure 9. (top) Bounce-averaged whistler-chorus energy diffusion coefficients D_{EE} and (bottom) momentum-diffusion coefficients D_{PP} for electrons in the dayside magnetosphere are plotted as functions of the equatorial pitch angle. The D_{EE} coefficients are calculated in Horne et al. (2013), and the D_{PP} coefficients are calculated from the D_{EE} coefficients.

declining in magnitude near $\alpha = 90^\circ$ for low energies and $D_{PP}(\alpha)$ declining in magnitude near $\alpha = 0^\circ$ for high energies. In the momentum-diffusion simulations, that region $20^\circ < \alpha < 80^\circ$ is fit by a constant value:

$$D_{PP} = 7.1 \times 10^{-39} \quad \text{for } E > 200 \text{ keV} \quad (9a)$$

$$D_{PP} = 1.4 \times 10^{-39} + \frac{(E - 60)}{140} 5.7 \times 10^{-39} \quad \text{for } 200 \text{ keV} < E < 60 \text{ keV} \quad (9b)$$

$$D_{PP} = 1.4 \times 10^{-39} \quad \text{for } E < 60 \text{ keV}, \quad (9c)$$

where D_{PP} has units of $(\text{gm cm/s})^2 \text{ s}^{-1}$ and where the electron energy E is in keV. The $D_{PP}(E)$ values of expression (9) will be taken to be independent of the pitch angle α . Along with this approximation, the coefficients $D_{P\alpha}$ and $D_{\alpha P}$ are ignored. Using expressions (9a)–(9c) for D_{PP} , the momentum-diffusion equation of expression (7) is computationally solved using the methodology of Borovsky and Eilek (1986). The quantity $n(p) \equiv 4\pi p^2 f(p)$ is defined, and with this definition expression (7) becomes the parabolic equation

$$\frac{\partial n}{\partial t} = \frac{\partial}{\partial p} \left[D_{PP} \frac{\partial n}{\partial p} + H n \right], \quad (10)$$

where $H \equiv -2D_{PP}/p$ and $D_{PP} = D_{PP}(p)$. Expression (10) is solved on the $\alpha = \text{constant}$ rows of the p - α grid with the numerical scheme of Borovsky and Eilek (1986), which includes a truncation-interpolation scheme

pumping (solid curves) and also after 1 h and 6 h for the 200 keV seed population (dashed blue curves). As can be seen, the magnetic pumping process catalyzed by chorus waves can produce energetic electrons from the low-energy seed population with kinetic energies of an order of magnitude larger than the seed population. The blue curves of Figure 8 show the temporal growth of the high-energy tail as the tail becomes more robust with time.

Note that since the pitch angle diffusion coefficient $D_{\alpha\alpha}$ for EMIC waves is zero for energies less than 400 keV, the EMIC-catalyzed magnetic pumping process cannot energize seed electrons into high-energy radiation belt electrons.

5. Comparison With Chorus Wave Energy Diffusion

For a comparison of the action of compressional magnetic pumping with direct energy diffusion by chorus waves, the results of magnetic pumping simulations are compared with the results of momentum-diffusion calculations for chorus waves. On a two-dimensional grid (as in Figure 2) in p versus α the momentum-diffusion equation

$$\frac{\partial f}{\partial t} = \frac{1}{p^2} \frac{\partial}{\partial p} \left[p^2 D_{PP} \frac{\partial f}{\partial p} \right] \quad (7)$$

is numerically solved using the energy diffusion coefficients D_{EE} of Horne et al. (2013), and the pitch angle diffusion equation (expression (2)) is numerically solved using the pitch angle diffusion coefficients $D_{\alpha\alpha}$ of Horne et al. (2013). The same chorus wave conditions are used as in the magnetic pumping calculations: upper band and lower band chorus for $Kp > 4$ at $L^* = 6.5$ in the 9–12 LT sector. The $D_{EE}(E, \alpha)$ coefficients of Horne et al. (2013) are plotted in Figure 9a in units of $\text{keV}^2 \text{ s}^{-1}$. Using equation (29) of Glauert and Horne (2005)

$$D_{PP} = \frac{1}{c^2} \frac{(E + E_0)^2}{E(E + 2E_0)} D_{EE}, \quad (8)$$

the momentum-diffusion coefficients D_{PP} are obtained from D_{EE} . In Figure 9b the momentum-diffusion coefficients $D_{PP}(E, \alpha)$ are plotted in units of $(\text{gm cm/s})^2 \text{ s}^{-1}$. It is seen that $D_{PP}(\alpha)$ has a flat region, with $D_{PP}(\alpha)$

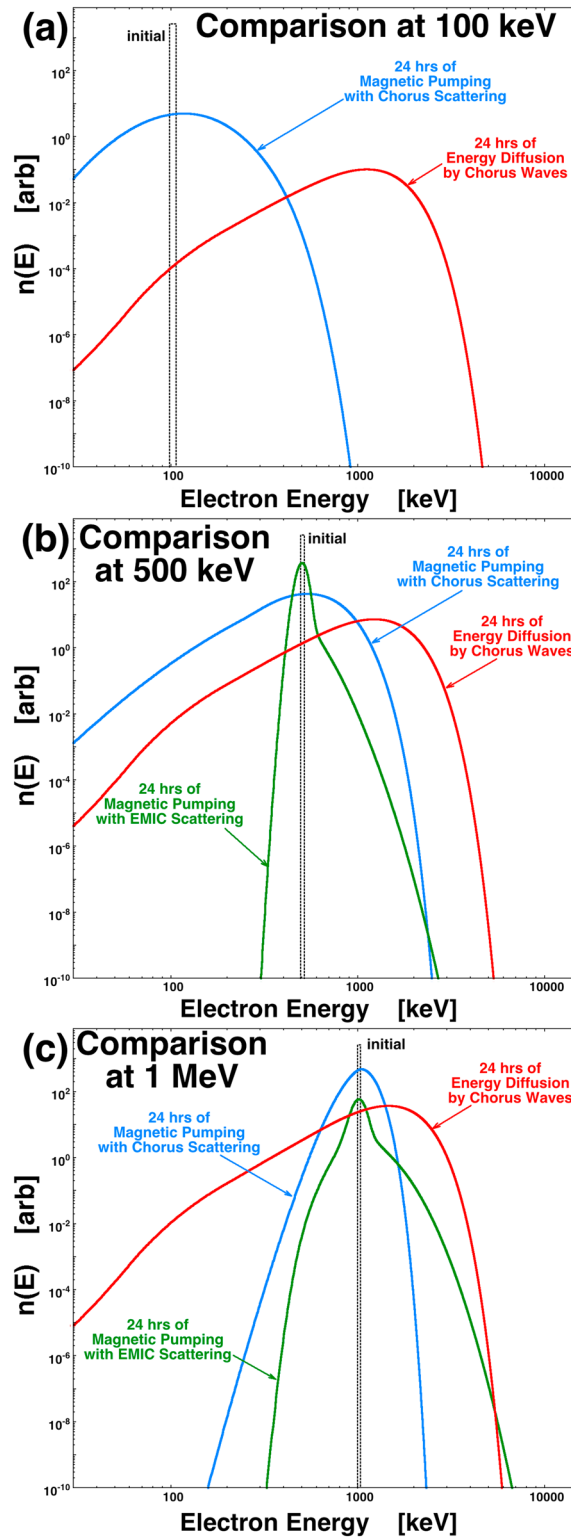


Figure 10. Initial value simulations are run for (a) 100 keV electrons, (b) 500 keV electrons, and (c) 1 MeV electrons. The black dashed curves are the initial energy distributions, and the solid curves are the distributions after 1 day of chorus-catalyzed magnetic pumping with a $2,401 \times 91$ grid (blue), after 1 day of EMIC-catalyzed magnetic pumping with a $3,601 \times 91$ grid (green), and after 1 day of whistler-chorus energy diffusion with a $10,001 \times 91$ grid (red). The atmospheric loss cone was operating in all of the simulations, and the plotted curves are integrated over all pitch angles.

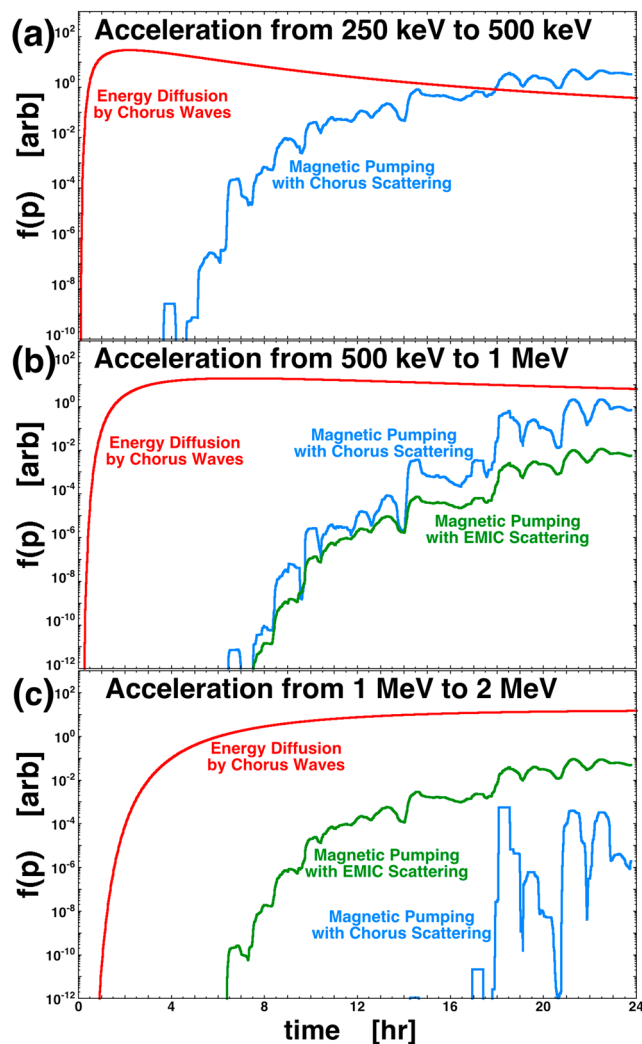


Figure 11. Phase-space densities at fixed energies are examined at 500 keV, 1 MeV, and 2 MeV for electrons starting out at (a) 250 keV, (b) 500 keV, and (c) 1 MeV, respectively. Initial value simulations are run for chorus-catalyzed magnetic pumping with a $2,401 \times 91$ grid (blue curves), for EMIC-catalyzed magnetic pumping with a $3,601 \times 91$ grid (green curves), and for whistler-chorus energy diffusion with a $10,001 \times 91$ grid (red curves). The atmospheric loss cone was operating in all of the simulations, and the plotted curves are integrated over all pitch angles.

at the high-momentum boundary to reduce boundary effects in the parabolic differential equation. In a single 1 min time step, the momentum-diffusion equation (expression (10)) is solved on the $\alpha = \text{constant}$ rows of the grid for 1 min worth of momentum diffusion, and then the pitch angle diffusion equation (expression (4)) is solved on the $p = \text{constant}$ columns of the grid for 1 min worth of pitch angle diffusion. This 1 min time step is repeated 1,440 times to estimate the evolution of an initial distribution of electrons after 1 day under the action of chorus wave energy diffusion and chorus wave pitch angle scattering into the loss cone.

In Figure 10 the initial-value-problem evolution of energy slice distribution functions (black dashed curves) under the action of 1 day of chorus wave momentum diffusion is plotted in red. The initial slice energies are 100 keV in Figure 10a, 500 keV in Figure 10b, and 1 MeV in Figure 10c. For comparison the evolution of the black initial energy slices after 1 day of chorus-catalyzed magnetic pumping is plotted in blue, and the evolution after 1 day of EMIC-catalyzed magnetic pumping is plotted in green. Note that EMIC-catalyzed magnetic pumping does not act on electrons with energies less than 400 keV. Comparing the red and blue curves in Figure 10, the energy diffusion (red) by chorus waves clearly produces a more robust population of energetic electrons than does chorus-catalyzed magnetic pumping (blue) for all of the energy slices shown. Comparing the red and green curves in Figure 10b, for initial electron energies of 500 keV chorus wave energy diffusion (red) produces a more robust population of energetic electrons than does EMIC-catalyzed magnetic pumping (green). For initial energies of 1 MeV (Figure 10a) EMIC-catalyzed magnetic pumping and chorus wave energy diffusion both produce strong energetic electron populations.

In Figure 11 magnetic pumping is again compared with energy diffusion by chorus waves, this time by examining the phase-space density of electrons at fixed energies. In each of the three panels of Figure 11 an initial isotropic distribution of electrons with a narrow range of energies is used as input to initial-value-problem simulations, and the phase-space density at a higher kinetic energy is examined. In Figure 11a the initial energies are from 242 keV to 260 keV, in Figure 11b the initial energies are from 493 keV to 517 keV, and in Figure 11c the initial energies are from 986 keV to 1,013 keV. In the simulations of Figure 11 the loss cone operates at all times. Figure 11a examines the energization from 250 keV to 500 keV: plotted in blue is the pitch angle-averaged phase-space density at 500 keV in the chorus-catalyzed magnetic pumping simulation and in red the pitch angle-averaged phase-space density at 500 keV in the chorus wave energy diffusion simulation. The blue curve in Figure 11a is irregular because the phase-space density at fixed energy varies in time as the magnetic field is compressed and decompressed. Note the rapidity of the energization from 250 keV to 500 keV in the energy diffusion simulation. Figure 11b examines the energization from 500 keV to 1 MeV: the blue curve is for chorus-catalyzed magnetic pumping, the green curve is for EMIC-catalyzed magnetic pumping, and the red curve is for chorus wave energy diffusion. Note again the rapidity of the energization in the energy diffusion simulation. In Figure 11b the chorus-catalyzed and the EMIC-catalyzed magnetic pumping are similar in their abilities to energize electrons from 500 keV to 1 MeV. (Dependent on the amplitude of chorus and EMIC waves.) Figure 11c examines the energization from 1 MeV to 2 MeV: the blue curve is for chorus-catalyzed pumping, the green curve is for EMIC-catalyzed pumping, and the red curve is for chorus wave energy diffusion. Again the chorus wave energy diffusion (red) provides the most rapid energization, followed by the EMIC-catalyzed magnetic pumping (green). Figure 11 verifies the finding that compressional magnetic pumping is not as powerful as chorus wave energy diffusion for energizing electrons.

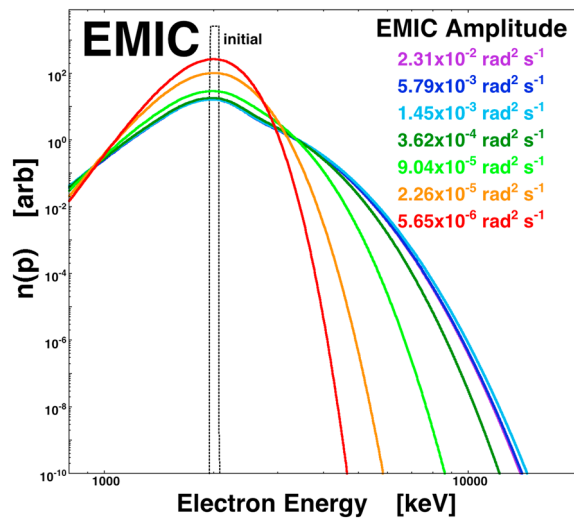


Figure 12. Seven initial value simulations of compressional magnetic pumping of electrons catalyzed by EMIC pitch angle scattering. The dashed black curve is the initial energy distribution (isotropic in pitch angle) of electrons in all seven simulations. The seven solid curves are the electron energy distributions after 1 day of compressional magnetic pumping with seven different amplitudes for the EMIC waves. The simulation grids were $3,601 \times 91$ grid points in p and α . The atmospheric loss cone was operating in all of the simulations, and the plotted curves are integrated over all pitch angles.

For the parameters used in these simulations, compressional magnetic pumping in the dayside magnetosphere at geosynchronous orbit during high-speed stream-driven storms is not as strong producer of energetic electrons as is chorus wave energy diffusion.

6. Discussion

Compressional magnetic pumping does not appear to be a dominant mechanism for energizing the outer electron radiation belt during high-speed stream-driven storms. In section 5 it was found that chorus wave energy diffusion produces a much more robust energetic electron population from lower energy electrons. For the production of a high-energy tail on the electron energy distribution, EMIC-catalyzed magnetic pumping is more efficient than is chorus-catalyzed magnetic pumping. Since EMIC waves are much less efficient at directly accelerating electrons than are chorus waves (cf. Glauert and Horne, 2005; Horne and Thorne, 1998), it is possible that compressional magnetic pumping could be a dominant energization mechanism in the dayside magnetosphere if EMIC waves are present and chorus waves are not. In some locations this is possible: near geosynchronous orbit EMIC is mainly observed at local noon and in the afternoon (e.g., Anderson et al., 1992; Bossen et al., 1976), while chorus amplitudes are weak in the afternoon sector (e.g., Horne, Thorne, Glauert, et al., 2005; Horne et al., 2013). The efficiency of EMIC-catalyzed magnetic pumping for producing energetic electrons is somewhat insensitive to the EMIC wave amplitudes over a large range of amplitudes as

shown in Figure 12 where a 2 MeV initial distribution of electrons is subjected to 1 day of compressional magnetic pumping catalyzed by EMIC waves with different amplitudes as gauged by the value of D_0 in expressions (6a)–(6g).

With strong enough $\Delta B/B$ compressions by the solar wind, compressional magnetic pumping could be the dominant energization mechanism in the dayside magnetosphere. At geosynchronous orbit during typical high-speed stream-driven storms this is not likely to be the case, but during sheath-driven storms it might be. In Figure 13 (top) the superposed epoch average of the 10 min change in the solar wind ram pressure $\Delta P_{\text{ram}10}$ (as measured by the Solar Wind Electron Proton Alpha Monitor instrument, McComas et al., 1998, on ACE) is plotted in blue for 70 high-speed stream-driven storms and in red for 47 coronal mass ejection (CME) sheaths. The zero epoch for the blue curve is the onset of the high-speed stream-driven storm, which occurs while a corotating interaction region (CIR) is passing the Earth; the zero epoch for the red curve is the passage of an interplanetary shock, which forms the leading edge of a CME sheath. Figure 13 (top) demonstrates that the temporal variations of the solar wind ram pressure are much greater on average in CME sheaths than they are in CIRs. In Figure 13 (bottom) the superposed average of the 10 min change $\Delta B_{10}/B$ in the magnetic field strength at geosynchronous orbit in the dayside magnetosphere is plotted as measured by the fluxgate magnetometer (Dunham et al., 1996) on the GOES spacecraft. Again, the zero epoch for the blue curve is the onset of the high-speed stream-driven storm, and the zero epoch for the red curve is the passage of an interplanetary shock. As seen in Figure 13 (bottom), on average the fractional compression of the dayside magnetic field by the solar wind is about a factor of 2 greater during CME sheaths than it is during CIRs. A factor of 2 increase in $\Delta B/B$ produces a factor of 4 increase in the speed of compressional magnetic pumping. Depending on the strength of EMIC in the dayside magnetosphere during sheath-driven storms, compressional magnetic pumping might be the dominant energization mechanism operating on the electron radiation belt.

The effectiveness of compressional magnetic pumping for the production of energetic electrons is probably limited to geosynchronous orbit ($r = 6.6 R_E$) and outward. The efficiency of compressional pumping goes as $(\Delta B/B_0)^2$ where ΔB is the amplitude of the magnetic compressions and B_0 is the mean magnetic field strength. The large spatial extents in the east-west and north-south directions of the Chapman-Ferraro current sheet on the dayside magnetopause that produces the ΔB in the dayside magnetosphere means that the amplitude of ΔB is not very sensitive to the radial distance from the Chapman-Ferraro current sheet.

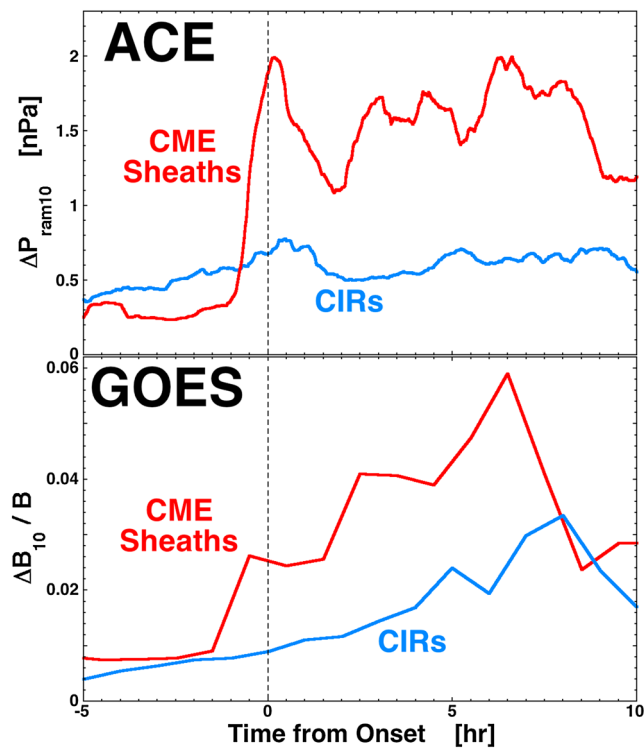


Figure 13. (top) The superposed epoch average of the 10 min change in the solar wind ram pressure ΔP_{ram10} as measured by ACE is plotted. (bottom) The superposed epoch average of the 10 min change $\Delta B_{10}/B$ in the dayside magnetic field strength at geosynchronous orbit as measured by the GOES spacecraft is plotted. In both panels the blue curves are for 70 high-speed stream-driven storms, and the red curves are for 47 coronal mass ejection (CME) sheaths. The zero epoch for the blue curves is the onset of the high-speed stream-driven storm, and the zero epoch for the red curves is the passage of an interplanetary shock.

However, B_o varies approximately as r^3 in the dayside magnetosphere, where r is the distance from the Earth. Hence, $(\Delta B/B_o)^2$ is reduced very strongly going toward the Earth. Going outward from geosynchronous orbit, $(\Delta B/B_o)^2$ increases substantially, but the trapping of the radiation belt electrons in this regions may be weak. Hence, compressional magnetic pumping may be very strong beyond geosynchronous orbit, and the radiation belt population may be tenuous.

Compressional magnetic pumping should also act on the proton radiation belt with pitch angle scattering occurring via proton interactions with EMIC waves (Shoji & Omura, 2012; Søråas et al., 1999) or with whistler-mode hiss (Kozyra et al., 1994; Villalon & Burke, 1994). Examining the proton radiation belt at geosynchronous orbit during 94 high-speed stream-driven storms, Borovsky et al. (2016) found that the flux of 1 MeV protons systematically increases in the day prior to the onset of a high-speed stream-driven storm. At such times before the storm onset, (1) the solar wind passing the Earth is often sector reversal region plasma that is very inhomogeneous (Borriani et al., 1981; Gosling et al., 1981) with strong temporal variations in the solar wind ram pressure, and (2) the plasmopause often extends to beyond geosynchronous orbit owing the refilling of the outer plasmasphere (Borovsky & Steinberg, 2006; Denton & Borovsky, 2008). These two factors may combine to produce strong $\Delta B/B$ in the dayside magnetosphere with whistler-mode hiss scattering of the protons.

In this report an assessment was made about the importance of compressional magnetic pumping in the dayside magnetosphere for the evolution of the outer electron radiation belt. The study was restricted to the dayside magnetosphere where the magnetic field strength variations ΔB that an electron experiences could be estimated. Before compressional magnetic pumping can be assessed for the electron radiation belt in the nightside magnetosphere, an estimate of the time variability of ΔB as seen by an electron in the nightside magnetosphere must be obtained. Assessing ΔB as seen by an electron in the nightside magnetosphere might require a

program of research that combines global MHD simulations of the dynamic solar wind-driven magnetosphere with spacecraft magnetic field measurements in the nightside outer radiation belt.

7. Summary and Future

This investigation computationally explored the magnetic pumping of radiation belt electrons associated with compressions of the dayside magnetosphere driven by temporal changes in the solar wind. Chorus-catalyzed magnetic pumping and EMIC-catalyzed magnetic pumping were separately simulated. The magnetic pumping simulation results were compared with energy diffusion calculations for chorus waves in the dayside magnetosphere. The parameters chosen for the simulations pertain to the early phase of high-speed stream-driven storms.

The findings of this investigation are the following.

1. If both pitch angle scattering of electrons and magnetic compressions are present, the magnetic pumping energization of electrons is unavoidable.
2. Loss cone losses of electrons operate during the magnetic pumping energization process. When pitch angle scattering is efficient near 0° pitch angles (chorus waves acting on lower energy (seed) electrons and EMIC waves acting on higher-energy electrons), the diffusion into the loss cone is more robust.
3. Chorus-catalyzed magnetic pumping and EMIC-catalyzed magnetic pumping both produce an increase in the average energy of electrons. This increase is a combination of heating of the electron distribution by magnetic pumping and the stronger loss of lower energy electrons into the loss cone.
4. Both chorus-catalyzed and EMIC-catalyzed magnetic pumping produce energetic electron populations from lower energy electrons.

5. Chorus-catalyzed magnetic pumping is more efficient at energizing medium-energy (50 keV to 200 keV) electrons than it is at energizing higher-energy (500 keV to 2 MeV) electrons.
6. EMIC-catalyzed magnetic pumping does not operate on electrons with kinetic energies below about 400 keV.
7. For higher-energy electrons (500 keV to 2 MeV), EMIC-catalyzed magnetic pumping produces more energetic electrons than does chorus-catalyzed magnetic pumping.
8. The simulation results of compressional magnetic pumping were compared with numerical calculations of direct energy diffusion by chorus waves. In general, compressional magnetic pumping is less efficient at energizing electrons than is chorus energy diffusion. The strength of this conclusion, however, depends on the amplitude $\Delta B/B$ of the dayside magnetic field compressions and on the amplitudes of chorus and EMIC waves.
9. Compressional magnetic pumping catalyzed by chorus wave or EMIC wave pitch angle scattering is probably a minor contributor to the energization of the outer electron radiation belt during high-speed stream-driven storms.
10. Inward of geosynchronous orbit magnetic pumping will be much less effective.

Four future studies are suggested: (1) an assessment of the role of compressional magnetic pumping on the electron radiation belt during CME sheath-driven storms, (2) an assessment of the compressional magnetic pumping of the proton radiation belt prior to the onset of high-speed stream-driven storms, (3) a determination of the magnetic field compressions that electrons undergo in the nightside magnetosphere, and (4) an analysis of compressional magnetic pumping in the nightside magnetosphere.

Acknowledgments

The authors thank Mick Denton, Sarah A. Glauert, Mike Hartinger, Mike Henderson, Tobias Kersten, and Geoff Reeves for help and for helpful conversations. This work was supported at the University of Michigan by the NASA Geospace SR&T program via grant NNX12AD29G; supported at the Space Science Institute by the NASA Heliophysics LWS TRT program via grants NNX14AN90G and NNX16AB75G, by the NSF GEM program via award AGS-1502947, by the NSF Solar-Terrestrial program via grant AGS-1261659, and by the NASA Heliophysics Guest Investigator program via grant NNX14AC15G; and supported at the British Antarctic Survey by UK Natural Environment Research Council National Capability funding. Simulation outputs are available upon request from the first author. J. E. B. dedicates this paper to Glenn Joyce and Chris Goertz.

References

- Albert, J. M. (2008). Efficient approximations of quasi-linear diffusion coefficients in the radiation belt. *Journal of Geophysical Research*, *113*, A06208. <https://doi.org/10.1029/2007JA012936>
- Alfvén, H. (1950). On the origin of cosmic radiation. II. *Physical Review*, *77*, 375–379.
- Alfvén, H. (1954). On the origin of cosmic radiation. *Tellus*, *6*, 232–253.
- Alfvén, H. (1959). Momentum spectrum of the Van Allen radiation. *Physical Review Letters*, *3*, 459–460.
- Alfvén, H., & Fälthammar, C.-G. (1963). *Cosmical electrodynamics, Sect. 2.7* (Vol. 4). New York: Oxford University Press.
- Anderson, B. J., Erlandson, R. E., & Zanetti, L. J. (1992). A statistical study of Pc 1–2 magnetic pulsations in the equatorial magnetosphere 1. Equatorial occurrence distribution. *Journal of Geophysical Research*, *97*, 3075–3101.
- Artemyev, A. V., Agapitov, O. V., Mourenas, D., Karasnoselskikh, V. V., & Mozer, F. S. (2015). Wave energy budget analysis in the Earth's radiation belts uncovers a missing energy. *Nature Communications*, *6*, 7143.
- Balikhin, M. A., Boynton, R. J., Walker, S. N., Borovsky, J. E., Billings, S. A., & Wei, H. L. (2011). Using the NARMAX approach to model the evolution of energetic electrons fluxes at geostationary orbit. *Geophysical Research Letters*, *38*, L18105. <https://doi.org/10.1029/2011GL048980>
- Birn, J., Thomsen, M. F., Borovsky, J. E., Reeves, G. D., & Hesse, M. (2000). Particle acceleration in the dynamic magnetotail. *Physics Plasmas*, *7*, 2149–2156.
- Birn, J., Thomsen, M. F., Borovsky, J. E., Reeves, G. D., McComas, D. J., Belian, R. D., & Hesse, M. (1998). Substorm electron injections: Geosynchronous observations and test particle simulations. *Journal of Geophysical Research*, *103*, 9235–9248.
- Borovsky, J. E. (1986). Magnetic pumping by magnetosonic waves in the presence of noncompressive electromagnetic fluctuations. *Physics of Fluids*, *29*, 3245–3260.
- Borovsky, J. E. (1988). Induced absorption of extraordinary (Z-mode) waves by electron pumping. *Physics of Fluids*, *31*, 700–702.
- Borovsky, J. E. (2017). Time-integral correlations of multiple variables with the relativistic-electron flux at geosynchronous orbit: The strong roles of the substorm-injected electrons and the ion plasma sheet. *Journal of Geophysical Research: Space Physics*, *122*. <https://doi.org/10.1002/2017JA024476>
- Borovsky, J. E., Cayton, T. E., Denton, M. H., Belian, R. D., Christensen, R. A., & Ingraham, J. C. (2016). The proton and electron radiation belts at geosynchronous orbit: Statistics and behavior during high-speed-stream-driven storms. *Journal of Geophysical Research: Space Physics*, *121*, 5449–5488. <https://doi.org/10.1002/2016JA022520>
- Borovsky, J. E., & Denton, M. H. (2006). The differences between CME-driven storms and CIR-driven storms. *Journal of Geophysical Research*, *111*, A07508. <https://doi.org/10.1029/2005JA011447>
- Borovsky, J. E., & Denton, M. H. (2010a). On the heating of the outer radiation belt to produce high fluxes of relativistic electrons: Measured heating rates for high-speed-stream-driven storms. *Journal of Geophysical Research*, *115*, A12206. <https://doi.org/10.1029/2010JA015342>
- Borovsky, J. E., & Denton, M. H. (2010b). The magnetic field at geosynchronous orbit during high-speed-stream-driven storms: Connections to the solar wind, the plasma sheet, and the outer electron radiation belt. *Journal of Geophysical Research*, *115*, A08217. <https://doi.org/10.1029/2009JA015116>
- Borovsky, J. E., & Denton, M. H. (2011). A survey of the anisotropy of the outer electron radiation belt during high-speed-stream-driven storms. *Journal of Geophysical Research*, *116*, A05201. <https://doi.org/10.1029/2010JA016151>
- Borovsky, J. E., & Denton, M. H. (2013). The differences between storms driven by helmet-streamer CIRs and storms driven by pseudostreamer CIRs. *Journal of Geophysical Research: Space Physics*, *118*, 5506–5521. <https://doi.org/10.1002/jgra.50524>
- Borovsky, J. E., & Denton, M. H. (2014). Exploring the cross-correlations and autocorrelations of the ULF indices and incorporating the ULF indices into the systems science of the solar-wind-driven magnetosphere. *Journal of Geophysical Research: Space Physics*, *119*, 4307–4334. <https://doi.org/10.1002/2014JA019876>
- Borovsky, J. E., & Denton, M. H. (2016). Compressional perturbations of the dayside magnetosphere during high-speed-stream-driven geomagnetic storms. *Journal of Geophysical Research: Space Physics*, *121*, 4569–4589. <https://doi.org/10.1002/2015JA022136>

- Borovsky, J. E., & Eilek, J. A. (1986). A study of the stochastic energization of charged particles with and without synchrotron energy loss. *Astrophysical Journal*, *308*, 929–953.
- Borovsky, J. E., Friedel, R. H. W., & Denton, M. H. (2014). Statistically measuring the amount of pitch-angle scattering that energetic electrons undergo as they drift across the plasmaspheric drainage plume at geosynchronous orbit. *Journal of Geophysical Research: Space Physics*, *119*, 1814–1826. <https://doi.org/10.1002/2013JA019310>
- Borovsky, J. E., Goertz, C. K., & Joyce, G. (1981). Magnetic pumping of particles in the outer Jovian magnetosphere. *Journal of Geophysical Research*, *86*, 3481–3495.
- Borovsky, J. E., & Hansen, P. J. (1990). The magnetic pumping of plasmas with sawtooth waveforms. *Physics of Fluids B*, *2*, 1114–1127.
- Borovsky, J. E., & Hansen, P. J. (1991). The breaking of the first adiabatic invariants of particles in time-dependent magnetic fields: Computer simulations and theory. *Physical Review A*, *43*, 5605–5627.
- Borovsky, J. E., & Steinberg, J. T. (2006). The “calm before the storm” in CIR/magnetosphere interactions: Occurrence statistics, solar-wind statistics, and magnetospheric preconditioning. *Journal of Geophysical Research*, *111*, A07S10. <https://doi.org/10.1029/2005JA011397>
- Borovsky, J. E., & Yakymenko, K. (2017). Substorm occurrence rates, substorm recurrence times, and solar-wind structure. *Journal of Geophysical Research: Space Physics*, *122*, 2973–2998. <https://doi.org/10.1002/2016JA023625>
- Borini, G., Gosling, J. T., Bame, S. J., Feldman, W. C., & Wilcox, J. M. (1981). Solar wind helium and hydrogen structure near the heliospheric current sheet: A signal of coronal streamers at 1 AU. *Journal of Geophysical Research*, *86*, 4565–4573. <https://doi.org/10.1029/JA086iA06p04565>
- Bossen, M., McPherron, R. L., & Russell, C. T. (1976). A statistical study of Pc 1 pulsations at synchronous orbit. *Journal of Geophysical Research*, *81*, 6083–6091.
- Boynton, R. J., Balikhin, M. A., Billings, S. A., Reeves, G. D., Ganushkina, N., Gadalín, M., ... Walker, S. N. (2013). The analysis of electron fluxes at geosynchronous orbit employing a NARMAX approach. *Journal of Geophysical Research: Space Physics*, *118*, 1500–1513. <https://doi.org/10.1002/jgra.50192>
- Canobbio, E. (1972). Neoclassical theory of Landau damping and ion and electron transit-time magnetic pumping (TTMP) in toroidal geometry. *Nuclear Fusion*, *12*, 561–568.
- Cayton, T. E., Belian, R. D., Gary, S. P., Fritz, T. A., & Baker, D. N. (1989). Energetic electron components at geosynchronous orbit. *Geophysical Research Letters*, *16*, 147–150.
- Chan, K.-W., & Holzer, R. E. (1976). ELF hiss associated with plasma density enhancements in the outer magnetosphere. *Journal of Geophysical Research*, *81*, 2267–2274.
- Dai, L., Wygant, J. R., Cattell, C. A., Thaller, S., Derten, K., Beneman, A., ... Tao, X. (2014). Evidence for injection of relativistic electrons into the Earth's outer radiation belt via intense substorm electric fields. *Geophysical Research Letters*, *41*, 1133–1141. <https://doi.org/10.1002/2014GL059228>
- DeGeling, A. W., Ozeke, L. G., Rankin, R., Mann, I. R., & Kabin, K. (2008). Drift resonant generation of peaked relativistic electron distributions by Pc 5 ULF waves. *Journal of Geophysical Research*, *113*, A02208. <https://doi.org/10.1029/2007JA012411>
- Denton, M. H., & Borovsky, J. E. (2008). Superposed epoch analysis of high-speed-stream effects at geosynchronous orbit: Hot plasma, cold plasma, and the solar wind. *Journal of Geophysical Research*, *113*, A07216. <https://doi.org/10.1029/2007JA012998>
- Denton, M. H., & Borovsky, J. E. (2012). Magnetosphere response to high-speed solar wind streams: A comparison of weak and strong driving and the importance of extended periods of fast solar wind. *Journal of Geophysical Research*, *117*, A00L05. <https://doi.org/10.1029/2011JA017124>
- Denton, M. H., & Borovsky, J. E. (2017). The response of the inner magnetosphere to the trailing edges of high-speed solar-wind streams. *Journal of Geophysical Research: Space Physics*, *122*, 501–516. <https://doi.org/10.1002/2016JA023592>
- Denton, M. H., Borovsky, J. E., & Cayton, T. E. (2010). A density-temperature description of the outer electron radiation belt during geomagnetic storms. *Journal of Geophysical Research*, *115*, A01208. <https://doi.org/10.1029/2009JA014183>
- Dmitriev, A. V., Bakhareva, M. F., & Minaeva, Y. S. (2001). Electron acceleration by magnetic pumping on the tail magnetopause. *Advances in Space Research*, *28*, 807–812.
- Dunham, W. D., MacIntyre, S. A., & Upton, C. R. (1996). Design and performance of the GOES-8 high resolution magnetometer. *SPIE Proceedings*, *2812*, 365.
- Elkington, S. R., Hudson, M. K., & Chan, A. A. (1999). Acceleration of relativistic electrons via drift-resonant interaction with toroidal-mode PC-5 ULF oscillations. *Geophysical Research Letters*, *26*, 3273–3276.
- Elkington, S. R., Hudson, M. K., & Chan, A. A. (2003). Resonant acceleration and diffusion of outer zone electrons in an asymmetric geomagnetic field. *Journal of Geophysical Research*, *108*, 1116. <https://doi.org/10.1029/2001JA009202>
- Falthammer, C.-G., & Walt, M. (1969). Radial motion resulting from pitch-angle scattering of trapped electrons in the distorted geomagnetic field. *Journal of Geophysical Research*, *74*, 4184–4186.
- Fok, M.-C., Moore, T. E., & Spjeldvik, W. N. (2001). Rapid enhancement of radiation belt electron fluxes due to substorm depolarization of the geomagnetic field. *Journal of Geophysical Research*, *106*, 3873–3881.
- Friedel, R. H. W., Reeves, G. D., & Obara, T. (2002). Relativistic electron dynamics in the inner magnetosphere—A review. *Journal of Atmospheric and Solar-Terrestrial Physics*, *64*, 265–282.
- Glauert, S. A., & Horne, R. B. (2005). Calculation of pitch angle and energy diffusion coefficients with the PADIE code. *Journal of Geophysical Research*, *110*, A04206. <https://doi.org/10.1029/2004JA010851>
- Goertz, C. K. (1978). Energization of particles in Jupiter's outer magnetosphere. *Journal of Geophysical Research*, *83*, 3145–3150.
- Gosling, J. T., Borini, G., Asbridge, J. R., Bame, S. J., Feldman, W. C., & Hansen, R. T. (1981). Coronal streamers in the solar wind at 1 AU. *Journal of Geophysical Research*, *86*, 5438–5448.
- Hamlin, D. A., Karplus, R., Vik, R. C., & Watson, K. M. (1961). Mirror and azimuthal drift frequencies for geomagnetically trapped particles. *Journal of Geophysical Research*, *66*, 1–4.
- Harteringer, M. D., Turner, D. L., Plaschke, F., Angelopoulos, V., & Singer, H. (2013). The role of transient ion foreshock phenomena in driving Pc5 ULF wave activity. *Journal of Geophysical Research: Space Physics*, *118*, 299–312. <https://doi.org/10.1029/2012JA018349>
- Horne, R. B., Kersten, T., Glauert, S. A., Meredith, N. P., Boscher, D., Sicard-Piet, A., ... Li, W. (2013). A new diffusion matrix for whistler mode chorus waves. *Journal of Geophysical Research: Space Physics*, *118*, 6302–6318. <https://doi.org/10.1002/jgra.50594>
- Horne, R. B., Meredith, N. P., Glauert, S. A., Varotsou, A., Boscher, D., Thorne, R. M., ... Anderson, R. R. (2006). Mechanisms for the acceleration of radiation belt electrons. In B. Tsurutani, et al. (Eds.), *Recurrent magnetic storms, Geophysical Monograph Series 167* (pp. 151–173). Washington, DC: American Geophysical Union.
- Horne, R. B., & Thorne, R. M. (1998). Potential waves for relativistic electron scattering and stochastic acceleration during magnetic storms. *Geophysical Research Letters*, *25*, 3011–3014.

- Horne, R. B., Thorne, R. M., Glauert, S. A., Albert, J. M., Meredith, N. P., & Anderson, R. R. (2005). Timescale for radiation belt electron acceleration by whistler mode chorus waves. *Journal of Geophysical Research*, *110*, A03225. <https://doi.org/10.1029/2004JA010811>
- Horne, R. B., Thorne, R. M., Shprits, Y. Y., Meredith, N. P., Glauert, S. A., Smith, A. J., ... Decreau, P. M. (2005). Wave acceleration of electrons in the Van Allen radiation belts. *Nature*, *437*, 227–230.
- Ingraham, J. C., Cayton, T. E., Belian, R. D., Christensen, R. A., Friedel, R. H. W., Meier, M. M., ... Tuszewski, M. (2001). Substorm injection of relativistic electrons to geosynchronous orbit during the great magnetic storm of March 24, 1991. *Journal of Geophysical Research*, *106*, 25,759–25,776. <https://doi.org/10.1029/2000JA000458>
- Jordanova, V. K., Miyoshi, Y. S., Zaharia, S., Thomsen, M. F., Reeves, G. D., Evans, D. S., ... Fennell, J. F. (2006). Kinetic simulations of ring current evolution during the Geospace environment modeling challenge events. *Journal of Geophysical Research*, *111*, A11510. <https://doi.org/10.1029/2006JA011644>
- Kepko, L., & Spence, H. E. (2003). Observations of discrete, global magnetospheric oscillations directly driven by solar wind density variations. *Journal of Geophysical Research*, *108*, 1257. <https://doi.org/10.1029/2002JA009676>
- Kim, H.-J., Chan, A. A., Wolf, R. A., & Birn, J. (2000). Can substorms produce relativistic outer belt electrons? *Journal of Geophysical Research*, *105*, 7721–7735. <https://doi.org/10.1029/1999JA900465>
- Koehler, F., & Samain, A. (1971). New method of magnetic pumping for plasma heating. *Physical Review Letters*, *26*, 490.
- Kovalevskiy, I. V. (1980). Ion-cyclotron instability in the frontal boundary layer of the geomagnetosphere produced by detached plasma clouds. *Geomagnetism and Aeronomy*, *20*, 338.
- Kovalevskiy, I. V. (1981). Cyclotron instability during interaction of detached plasma regions with the plasma sheet during substorms. *Geomagnetism and Aeronomy*, *21*, 83.
- Kozyra, J. U., Rasmussen, C. E., Miller, R. H., & Lyons, L. R. (1994). Interaction of ring current and radiation belt protons with ducted plasmaspheric hiss 1. Diffusion coefficients and timescales. *Journal of Geophysical Research*, *99*, 4069–4084.
- Kozyreva, O., Piliipenko, V., Engebretson, M. J., Yumoto, K., Watermann, J., & Romanova, N. (2007). In search of a new ULF wave index: Comparison of Pc5 power with dynamics of geostationary relativistic electrons. *Planetary and Space Science*, *55*, 755–769.
- Kuijpers, J., Fletcher, L., Abada-Simon, M., Horne, K. D., Raadu, M. A., Ramsay, G., & Steeghs, D. (1997). Magnetic pumping in cataclysmic variable AE Aquarii. *Astronomy and Astrophysics*, *322*, 242–255.
- Lezniak, T. W., Arnoldy, R. L., Parks, G. K., & Winkler, J. R. (1968). Measurements and intensity of energetic electrons at the equator at $6.6 R_E$. *Radio Science*, *3*, 710–714.
- Li, L. Y., Cao, J. B., Yang, J. Y., & Dong, Y. X. (2013). Joint response of geosynchronous magnetic field and relativistic electrons to external changes in solar wind dynamic pressure and interplanetary magnetic field. *Journal of Geophysical Research: Space Physics*, *118*, 1472–1482. <https://doi.org/10.1002/jgra.50201>
- Liu, W. W., & Rostoker, G. (1995). Energetic ring current particles generated by recurring substorm cycles. *Journal of Geophysical Research*, *100*, 21,897–21,910.
- Liu, W. W., Rostoker, G., & Baker, D. N. (1999). Internal acceleration of relativistic electrons by large-amplitude ULF pulsations. *Journal of Geophysical Research*, *104*, 17,391–17,407. <https://doi.org/10.1029/1999JA900168>
- Lyons, L. R., Thorne, R. M., & Kennel, C. F. (1972). Pitch-angle diffusion of radiation belt electrons within the plasmasphere. *Journal of Geophysical Research*, *77*, 3455–3474.
- Mathie, R. A., & Mann, I. R. (2000). A correlation between extended intervals of ULF wave power and storm-time geosynchronous relativistic electron flux enhancements. *Geophysical Research Letters*, *27*, 3261–3264. <https://doi.org/10.1029/2000GL003822>
- Mathie, R. A., & Mann, I. R. (2001). On the solar wind control of Pc5 ULF pulsation power at mid-latitudes: Implications for MeV electron acceleration in the outer radiation belt. *Journal of Geophysical Research*, *106*, 29,783–29,796. <https://doi.org/10.1029/2001JA000002>
- McComas, D. J., Blame, S. J., Barker, P., Feldman, W. C., Phillips, J. L., Riley, P., & Griffee, J. W. (1998). The Solar Wind Electron Proton Alpha Monitor (SWEPAM) for the Advanced Composition Explorer. *Space Science Review*, *86*, 563–512.
- McDiarmid, I. B., & Burrows, J. R. (1965). On an electron source for the outer Van Allen radiation zone. *Canadian Journal of Physics*, *43*, 1161–1164.
- Melrose, D. B. (1969). Acceleration of ultrarelativistic electrons in the Crab Nebula. *Astrophysics and Space Science*, *4*, 165–181.
- Meredith, N. P., Horne, R. B., & Anderson, R. R. (2001). Substorm dependence of chorus amplitudes: Implications for the acceleration of electrons to relativistic energies. *Journal of Geophysical Research*, *106*, 13,165–13,178. <https://doi.org/10.1029/2000JA900156>
- Meredith, N. P., Horne, R. B., Iles, R. H. A., Thorne, R. M., Heynderickx, D., & Anderson, R. R. (2002). Outer zone relativistic electron acceleration associated with substorm-enhanced whistler mode chorus. *Journal of Geophysical Research*, *107*, 1144. <https://doi.org/10.1029/2001JA900146>
- Meredith, N. P., Horne, R. B., Lam, M. M., Denton, M. H., Borovsky, J. E., & Green, J. C. (2011). Energetic electron precipitation during high-speed solar wind stream driven storms. *Journal of Geophysical Research*, *116*, A05223. <https://doi.org/10.1029/2010JA016293>
- Meredith, N. P., Horne, R. B., Sicard-Piet, A., Boscher, D., Yearby, K. H., Li, W., & Thorne, R. M. (2012). Global model of lower band and upper band chorus from multiple satellite observations. *Journal of Geophysical Research*, *117*, A12209. <https://doi.org/10.1029/2012JA017978>
- Min, K., Lee, J., & Keika, K. (2010). Chorus wave generation near the dawnside magnetopause due to the drift shell splitting of substorm-injected electrons. *Journal of Geophysical Research*, *115*, A00102. <https://doi.org/10.1029/2010JA015474>
- Mourenas, D., Artemyev, A. V., Ma, Q., Agapitov, O. V., & Li, W. (2016). Fast dropouts of multi-MeV electrons due to combined effects of EMIC and whistler mode waves. *Geophysical Research Letters*, *43*, 4155–4163. <https://doi.org/10.1002/2016GL068921>
- Mu, J.-L. (1993). A new magnetic pumping accelerator of charged particles in Jupiter's magnetosphere. *Geophysical Research Letters*, *20*, 1463–1466.
- Murty, G. S., & Varma, R. K. (1958). Acceleration of cosmic radiation. *Physical Review*, *112*, 1789.
- Ozeke, L. G., Mann, I. R., Murphy, K. R., Rae, I. J., Milling, D. K., Elkington, S. R., ... Singer, H. J. (2012). ULF wave derived radiation belt radial diffusion coefficients. *Journal of Geophysical Research*, *117*, A04222. <https://doi.org/10.1029/2011JA017463>
- Paulikas, G. A., & Blake, J. B. (1976). Modulation of trapped energetic electrons at $6.6 R_E$ by the interplanetary magnetic field. *Geophysical Research Letters*, *3*, 277–280.
- Porazik, P., Johnson, J. R., Kaganovich, I., & Sanchez, E. (2014). Modification of the loss cone for energetic particles. *Geophysical Research Letters*, *41*, 8107–8113. <https://doi.org/10.1002/2014GL061869>
- Roederer, J. G., & Schulz, M. (1969). Effect of shell splitting on radial diffusion in the magnetosphere. *Journal of Geophysical Research*, *74*, 4117–4122.
- Roederer, J. G., & Zhang, H. (2014). *Dynamics of magnetically trapped particles*. Heidelberg: Springer.
- Romanova, N., & Piliipenko, V. (2009). ULF wave indices to characterize the solar wind-magnetosphere interaction and relativistic electron dynamics. *Acta Geophysica*, *57*, 158–170.

- Rostoker, G., Skone, S., & Baker, D. N. (1998). On the origin of relativistic electrons in the magnetosphere associated with some geomagnetic storms. *Geophysical Research Letters*, *25*, 3701–3704.
- Safrankova, J., Goncharov, O., Nemecek, Z., Prech, L., & Sibeck, D. G. (2012). Asymmetric magnetosphere deformation driven by hot flow anomaly(ies). *Geophysical Research Letters*, *39*, L15107. <https://doi.org/10.1029/2012GL052636>
- Sauvaud, J.-A., Walt, M., Delcourt, D., Benoist, C., Penou, E., Chen, Y., & Russell, C. T. (2013). Inner radiation belt particle acceleration and energy structuring by drift resonance with ULF waves during geomagnetic storms. *Journal of Geophysical Research: Space Physics*, *118*, 1723–1736. <https://doi.org/10.1002/jgra.50125>
- Schluter, A. (1957). Der gyro-relaxations-effect. *Zeitschrift für Naturforschung*, *12a*, 822.
- Shprits, Y. Y., Meredith, N. P., & Thorne, R. M. (2007). Parameterization of radiation belt electron loss timescales due to interactions with chorus waves. *Geophysical Research Letters*, *34*, L11110. <https://doi.org/10.1029/2006GL029050>
- Shoji, M., & Omura, Y. (2012). Precipitation of highly energetic protons by helium branch electromagnetic ion cyclotron triggered emissions. *Journal of Geophysical Research*, *117*, A12210. <https://doi.org/10.1029/2012JA017933>
- Søråas, F., Aarsnes, K., Lundblad, J. A., & Evans, D. S. (1999). Enhanced pitch angle scattering of protons at mid-latitudes during geomagnetic storms. *Physics and Chemistry of the Earth, Part C: Solar, Terrestrial and Planetary Science*, *24*, 287–292.
- Spasojevic, M., & Fuselier, S. A. (2009). Temporal evolution of proton precipitation associated with the plasmaspheric plume. *Journal of Geophysical Research*, *114*, A12201. <https://doi.org/10.1029/2009JA014530>
- Spitzer, L., & Witten, L. (1953). On the ionization and heating of a plasma (USAEC Report NYO-999, March 1953).
- Summers, D., Thorne, R. M., & Xiao, F. (1998). Relativistic theory of wave-particle resonant diffusion with application to electron acceleration in the magnetosphere. *Journal of Geophysical Research*, *103*, 20,487–20,500.
- Summers, D., Ni, B., Meredith, N. P., Horne, R. B., Thorne, R. M., Moldwin, M. B., & Anderson, R. R. (2008). Electron scattering by whistler-mode ELF hiss in plasmaspheric plumes. *Journal of Geophysical Research*, *113*, A04219. <https://doi.org/10.1029/2007JA012678>
- Tataronis, J. A., & Grossmann, W. (1976). On Alfvén wave heating and transit time magnetic pumping in the guiding-centre model of a plasma. *Nuclear Fusion*, *16*, 667.
- Thorne, R. M., Horne, R. B., Jordanova, V. K., Bortnik, J., & Glauert, S. (2006). Interaction of EMIC waves with thermal plasma and radiation belt particles. In K. Takahashi, P. J. Chi, R. E. Denton, & R. L. Lysak (Eds.), *Magnetospheric ULF waves* (p. 213). Washington, DC: American Geophysical Union.
- Thorne, R. M., Li, W., Ni, B., Ma, Q., Bortnik, J., Chen, L., . . . Kanekal, S. G. (2013). Rapid local acceleration of relativistic radiation-belt electrons by magnetospheric chorus. *Nature*, *504*, 411–414.
- Thorne, R. M., Ö'Brien, T. P., Shprits, Y. Y., Summers, D., & Horne, R. B. (2005). Timescale for MeV electron microburst loss during geomagnetic storms. *Journal of Geophysical Research*, *110*, A09202. <https://doi.org/10.1029/2004JA010882>
- Tu, W., Elkington, S. R., Li, X., Liu, W., & Bonnell, J. (2012). Quantifying radial diffusion coefficients of radiation belt electrons based on global MHD simulation and spacecraft measurements. *Journal of Geophysical Research*, *117*, A10201. <https://doi.org/10.1029/2012JA017901>
- Ukhorskiy, A. Y., Shprits, Y. Y., Anderson, B. J., Takahashi, K., & Thorne, R. M. (2010). Rapid scattering of radiation belt electrons by short-time EMIC waves. *Geophysical Research Letters*, *37*, L09101. <https://doi.org/10.1029/2010GL042906>
- Viall, N. M., Kepko, L., & Spence, H. E. (2009). Relative occurrence rates and connection of discrete frequency oscillations in the solar wind density and dayside magnetosphere. *Geophysical Research Letters*, *114*, A01201. <https://doi.org/10.1029/2008JA013334>
- Villalon, E., & Burke, W. J. (1994). Diffusion of radiation belt protons by whistler waves. *Journal of Geophysical Research*, *99*, 21,329–21,340.
- Wing, S., & Sibeck, D. G. (1997). Effects of interplanetary magnetic field Z component and the solar wind dynamic pressure on the geosynchronous magnetic field. *Journal of Geophysical Research*, *102*, 7207–7216. <https://doi.org/10.1029/97JA00150>